Nucleon-nucleon bremsstrahlung at intermediate energies

V. Herrmann and J. Speth
Institut für Kernphysik, Forschungszentrum-Jülich, D-5170 Jülich, Germany

K. Nakayama
Department of Physics and Astronomy, University of Georgia, Athens, Georgia 30602 and Institut für Kernphysik, Forschungszentrum-Jülich D-5170 Jülich, Germany

(Received 20 October 1989)

Energetic photon production in proton-neutron as well as in proton-proton collisions at intermediate bombarding energies are investigated in a meson-exchange potential model calculation in an effort to provide a more reliable basis for calculations of hard photon production in heavy-ion collisions. Special attention is paid to the role of the one-body rescattering contribution, which has been neglected in previous work. It is shown that this contribution enhances the cross section for photon energies only near the maximum value allowed kinematically. As a function of photon energy, both *pn* and *pp* bremsstrahlung inclusive cross sections are shown to be rather flat except in the low photon energy region. The shape of the angular distribution is, to a large extent, determined by the convection current contribution, which in the soft-photon limit has a well-known dipole shape in the case of *pn* bremsstrahlung and a quadrupole shape in the case of *pp* bremsstrahlung. For photon energies above ~ 150 MeV where the magnetic current contribution dominates over the convection contribution, the shape of the angular distribution is roughly of a $\cos^2\theta$ form. The internal current gives rise to a nearly isotropic angular distribution. The $pp\gamma$ cross section is shown to be very small compared to the $pn\gamma$ cross section, even for considerably high-energy photons, because of the two-body current contribution, which is mostly absent in *pp* bremsstrahlung. The present calculation yields *np* bremsstrahlung cross sections which still tend to underpredict the data, although the measurements have large uncertainties.

I. INTRODUCTION

The observation of energetic photons produced in intermediate-energy heavy-ion collisions[1-4] has opened a new field of great interest in heavy-ion physics. The weakness of the electromagnetic interaction, combined with the fact that these photons are very energetic, makes them (the photons) a clean probe of the reaction dynamics. Theoretical calculations[5-8] using transport equations (such as the Boltzmann-Uhling-Uhlenbeck or Boltzmann master equation) to describe the heavy-ion dynamics give rise to photon cross sections which are in reasonable agreement with the experimental data. The basic ingredient in such calculations is the elementary proton-neutron (*pn*) bremsstrahlung process. Proton-proton (*pp*) bremsstrahlung is expected to play a minor role, at least in the region of photon energies covered by the existing heavy-ion data. Unfortunately, the scarcity of the *pn* bremsstrahlung data does not allow to provide the necessary information required in heavy-ion calculations. Therefore, all of these calculations rely on the theoretical prediction of the elementary *pn* bremsstrahlung process.

In an effort to provide a more reliable foundation for calculations of heavy-ion photoproduction, in the present work we investigate the elementary nucleon-nucleon (*NN*) bremsstrahlung inclusive processes. The *np* bremsstrahlung has been studied theoretically in the past[9,10] in an attempt to investigate the possible off-energy-shell behavior of the *NN* interaction which is not accessible with elastic scattering. However, the kinematical conditions considered in those works are quite different from those involved in heavy-ion experiments. Recently, in Ref. 11, we investigated some of the aspects of *pn* bremsstrahlung within conditions more suitable for application in heavy-ion calculations. In particular, we have shown that the two-body current is the dominant contribution for high-energy photons. In the present work we further analyze the elementary bremsstrahlung process for producing energetic photons. In particular, the rescattering contribution from the one-body current which was neglected in Ref. 11 will be investigated. In addition to *pn* bremsstrahlung, we also study *pp* bremsstrahlung. A few comparisons with the existing data are also presented. For the purpose of testing our numerical results, we compare the present calculations with earlier ones.

This paper is organized as follows: In Sec. II we present the necessary formulas for calculating the rescattering contribution from the different parts of the one-body current. A few numerical details are given in Appendix A. In Secs. III A and III B, selected results for *pn* and *pp* bremsstrahlung, respectively, are discussed. Section III C is devoted to the parametrization of the proton-neutron-photon ($pn\gamma$) amplitude following Ref.

12. Conclusions are given in Sec. IV. In Appendix B, a few details are given on how to construct the Lorentz-invariant transition amplitude from a nonrelativistic T matrix.

II. RESCATTERING FROM THE ONE-BODY CURRENT

Following Ref. 11, we write the transition amplitude M for producing a photon of momentum $\mathbf{k}$ and polarization ϵ in a NN collision as

$$M=\langle \epsilon,\mathbf{k};\phi_f|V_{\rm em}|0;\phi_i\rangle + \left\langle \epsilon,\mathbf{k};\phi_f\left|(T^-)^\dagger\frac{1}{E_f}V_{\rm em}\right|0;\phi_i\right\rangle + \left\langle \epsilon,\mathbf{k};\phi_f\left|V_{\rm em}\frac{1}{E_i}T^+\right|0;\phi_i\right\rangle + \left\langle \epsilon,\mathbf{k};\phi_f\left|(T^-)^\dagger\frac{1}{E_f}V_{\rm em}\frac{1}{E_i}T^+\right|0;\phi_i\right\rangle . \quad (2.1)$$

In the above equation, ϕ denotes the two-nucleon unperturbed wave function, E is the energy denominator, and $T^\pm$ stands for the T matrix. The subscript i (f) refers to the initial (final) two-nucleon state, while the superscript $+$ or $-$ indicates the boundary condition associated with the incoming ($+$) or outgoing ($-$) waves. $V_{\rm em}$ is the photon emission potential and it consists of three terms:[11]

$$V_{\rm em}=V_{\rm conv}+V_{\rm magn}+V_{\rm exch} , \quad (2.2)$$

where $V_{\rm conv}$ stands for the convection and $V_{\rm magn}$ for the magnetization current contribution; they constitute the one-body current. $V_{\rm exch}$ denotes the two-body current contribution and it is dominated by the meson-exchange current.[10]

In a previous work,[11] we calculated the bremsstrahlung amplitude as given by Eqs. (2.1) and (2.2) except for the rescattering contribution [the last term in Eq. (2.1)] from the one-body current, $V_{\rm conv}+V_{\rm magn}$. In Ref. 13 it is shown that, in the soft-photon approximation (SPA), a part of the rescattering term from the one-body current cancels the contribution from the two-body current, so that current conservation is preserved in that limit. Nevertheless, based on the results by Brown and Franklin[10] who found that it gives a minor influence to the cross sections, we had ignored that contribution entirely. This argument, however, has to be verified since the kinematical conditions in which we are interested are quite different from those studied in Ref. 10. In particular, we consider photons of much higher energies, where the rescattering contributions are expected to be more important. Therefore, in the present work, we also take into account this rescattering contribution. We note that the rescattering term from the two-body current was included in Ref. 11.

The rescattering contribution from the convection current in momentum space and in the initial NN center-of-mass (c.m.) frame reads

$$R_{\rm conv}=\left\langle \epsilon,\mathbf{k};\phi_{\mathbf{p}'}^{S'M_{S'}}\left|(T^-)^\dagger\frac{1}{E_f}V_{\rm conv}\frac{1}{E_i}T^+\right|0;\phi_{\mathbf{p}}^{SM_S}\right\rangle = -\sqrt{(2\pi)/k}\,\delta_{S'S}\sum_{M_{S''}}\int\frac{d^3p''}{(2\pi)^3}\frac{\epsilon\cdot\mathbf{p}''}{m}\left[\frac{e_1''}{D_-}\left\langle \mathbf{p}'-\frac{\mathbf{k}}{2},-\mathbf{p}'-\frac{\mathbf{k}}{2};SM_{S'}\left|(T^-)^\dagger\right|\mathbf{p}''-\mathbf{k},-\mathbf{p}'';SM_{S''}\right\rangle - \frac{e_2''}{D_+}\left\langle \mathbf{p}'-\frac{\mathbf{k}}{2},-\mathbf{p}'-\frac{\mathbf{k}}{2};SM_{S'}\left|(T^-)^\dagger\right|\mathbf{p}'',-\mathbf{p}''-\mathbf{k};SM_{S''}\right\rangle\right] \times\frac{1}{E(p'',p)}\langle \mathbf{p}'';SM_{S''}|T^+|\mathbf{p};SM_S\rangle . \quad (2.3)$$

In Eq. (2.3), S (S') and M_S ($M_{S'}$) denote total spin and its projection in the initial (final) state, m stands for the mass of the nucleon, and e_1'' and e_2'' are the electric charges of the interacting nucleons 1 and 2 (e for protons and 0 for neutrons). The double-primed quantities refer to the intermediate state. The relative momentum $\mathbf{p}$ ($\mathbf{p}'$) in the initial (final) state is related to the momenta of the nucleons $\mathbf{p}_1$ and $\mathbf{p}_2$ ($\mathbf{p}_1'$ and $\mathbf{p}_2'$) by

$$\mathbf{p}_1=\frac{\mathbf{P}}{2}+\mathbf{p},\quad \mathbf{p}_2=\frac{\mathbf{P}}{2}-\mathbf{p} , \quad (2.4a)$$

and

$$\mathbf{p}_1'=\frac{\mathbf{P}}{2}+\mathbf{p}'-\frac{\mathbf{k}}{2},\quad \mathbf{p}_2'=\frac{\mathbf{P}}{2}-\mathbf{p}'-\frac{\mathbf{k}}{2} , \quad (2.4b)$$

with $\mathbf{P}$ denoting the initial NN c.m. momentum. The energy denominators $D_\pm$ are given by

$$D_\pm=\varepsilon(|\mathbf{p}'-\mathbf{k}/2|)+\varepsilon(|\mathbf{p}'+\mathbf{k}/2|) -\varepsilon(p'')-\varepsilon(|\mathbf{p}'\pm\mathbf{k}/2|)+i\eta \quad (2.5a)$$

with

$$\varepsilon(p)=(p^2+m^2)^{1/2} . \quad (2.5b)$$

In the limit of $\mathbf{k}\to 0$, Eq. (2.5a) reduces to

$$D_\pm\equiv E(p'',p') =2[\varepsilon(p')-\varepsilon(p'')]+i\eta . \quad (2.5c)$$

In Ref. 11, Eq. (2.8a) should read as Eq. (2.5c), instead of

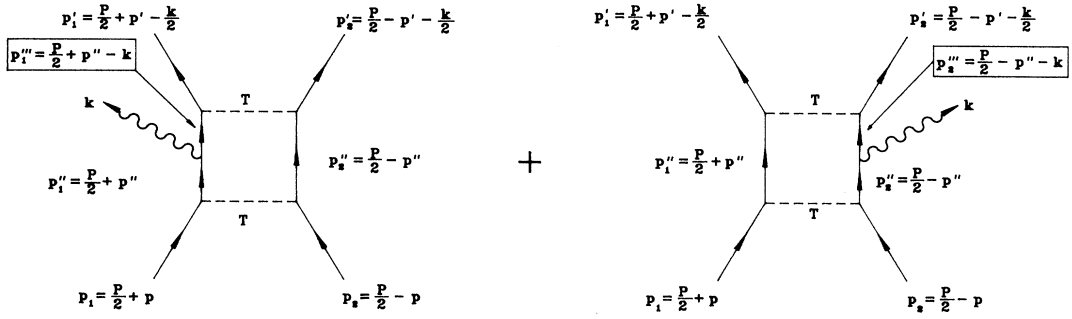

FIG. 1. One-body rescattering diagram for $NN\gamma$ to first order in the electromagnetic interaction. The dashed lines denote the NN T matrix and the wiggled lines represent the photon.

$$E(p',p)=2[\varepsilon(p')-\varepsilon(p)]+i\eta \ .$$

Also in Eq. (2.3) we have used the notation

$$\langle \mathbf{p}_1',\mathbf{p}_2';SM_{S'}|T|\mathbf{p}_1,\mathbf{p}_2;SM_S\rangle$$

for the arguments of the T-matrix elements. When the momenta of two interacting nucleons differ only by a sign, we use the usual notation of omitting one of the (momentum) arguments, such as in the last line in Eq. (2.3). A diagrammatic representation of the one-body rescattering amplitude and, in particular, of Eq. (2.3), is shown in Fig. 1.

The T-matrix elements in Eq. (2.3) may be easily transformed to any convenient Lorentz frame by noticing that

$$(\varepsilon_1'\varepsilon_2')^{1/2}\langle \mathbf{p}_1',\mathbf{p}_2';S'M_{S'}|T|\mathbf{p}_1,\mathbf{p}_2;SM_S\rangle\sqrt{\varepsilon_1\varepsilon_2}$$

is a Lorentz scalar (see Appendix B for details). Indeed,

$$\left\langle \mathbf{p}'-\frac{\mathbf{k}}{2},-\mathbf{p}'-\frac{\mathbf{k}}{2};S'M_{S'}\left|(T^-)^\dagger\right|\mathbf{p}''-\mathbf{k},-\mathbf{p}'';S''M_{S''}\right\rangle=\Lambda_-\left\langle \mathbf{p}';S'M_{S'}\left|(T^-)^\dagger\right|\mathbf{p}''-\frac{\mathbf{k}}{2};S''M_{S''}\right\rangle \tag{2.6a}$$

and

$$\left\langle \mathbf{p}'-\frac{\mathbf{k}}{2},-\mathbf{p}'-\frac{\mathbf{k}}{2};S'M_{S'}\left|(T^-)^\dagger\right|\mathbf{p}'',-\mathbf{p}''-\mathbf{k};S''M_{S''}\right\rangle=\Lambda_+\left\langle \mathbf{p}';S'M_{S'}\left|(T^-)^\dagger\right|\mathbf{p}''+\frac{\mathbf{k}}{2};S''M_{S''}\right\rangle , \tag{2.6b}$$

where $\Lambda_\pm$ is given by

$$\Lambda_\pm=\frac{\varepsilon(p')\varepsilon(|\mathbf{p}''\pm\mathbf{k}/2|)}{[\varepsilon(\mathbf{p}'')\varepsilon(|\mathbf{p}''\pm\mathbf{k}|)\varepsilon(|\mathbf{p}'-\mathbf{k}/2|)\varepsilon(|\mathbf{p}+\mathbf{k}/2|)]^{1/2}} \ . \tag{2.6c}$$

The T-matrix elements on the right-hand side of Eqs. (2.6a) and (2.6b) and the numerator in Eq. (2.6c) are expressed in the final NN c.m. frame, which is shifted by $-\mathbf{k}$ with respect to the initial NN c.m. frame.

We perform the integration over the momentum $\mathbf{p}''$ in Eq. (2.3) numerically, first integrating over the magnitude of $\mathbf{p}''$ ("radial" integral) and then over the solid angle. For most directions $\mathbf{p}''$ the integrand under the "radial" integral presents two poles for it contains a product of two energy denominators. However, since these poles are simple poles, we can always split the integral into two parts, each part having only one pole (see Appendix A for the details).

In the SPA, the angular integration in Eq. (2.3) can be carried out explicitly since, in this limit, Eq. (2.3) reduces to

$$R_{\rm conv}=-\sqrt{(2\pi)/k}\,\delta_{S',S}\sum_{M_{S''}}\int\frac{d^3p''}{(2\pi)^3}\frac{\boldsymbol{\epsilon}\cdot\mathbf{p}''}{m}(e_1''-e_2'')\left[\frac{\langle \mathbf{p}';SM_{S'}|(T^-)^\dagger|\mathbf{p}'';SM_{S''}\rangle\langle \mathbf{p}'';SM_{S''}|T^+|\mathbf{p};SM_S\rangle}{E(p'',p')E(p'',p)}\right] . \tag{2.7}$$

Using the standard partial-wave decomposition of the T matrix,[11] Eq. (2.7) becomes

$$\begin{aligned}R_{\rm conv}=&\sqrt{(2\pi)/k}\,\frac{1}{(2\pi)^3}\frac{2}{3\pi^2}\left[\frac{e}{m}\right]\delta_{S',S}\\&\times\sum i^{L''-L'}i^{L-L'''}(S'M_{S'}L'M_{L'}|J'M_{J'})(SM_SLM_L|JM_J)\\&\times Y_{L'M_{L'}}(\hat{p}')Y_{LM_L}(\hat{p})^*(-)^{S+M_J}[L''L'''JJ'](L'''0L''0|10)\begin{Bmatrix}J' & J & 1\\ L''' & L'' & S\end{Bmatrix}\\&\times\sum_\mu(-)^\mu\epsilon_{-\mu}(J-M_JJ'M_{J'}|1\mu)\delta_{T,T'\pm1}\int_0^\infty dp''p''^2T_{L''L'}^{J'S'T'}(p'',p')\frac{p''}{E(p'',p')E(p'',p)}T_{L'''L}^{JST}(p'',p) ,\end{aligned} \tag{2.8}$$

where J's, L's, and T's refer to the total angular momentum, the orbital momentum, and the total isospin of the states of the two interacting nucleons, respectively. M_J's and M_L's are the corresponding projections of total and orbital angular momenta. The unprimed (single-primed) quantities refer to the initial (final) state, while the double- and triple-primed ones refer to the intermediate states. The summation in the above equation runs over all J's, L's, the corresponding projections, and T's. Since all the T-matrix elements involved in Eq. (2.8) have the same boundary condition (+), we have dropped the superscript + for simplicity. We also introduced the notation $[j]\equiv\sqrt{2j+1}$.

It is clear from either Eq. (2.7) or (2.8) that the rescattering term from the convection current contributes only to the *pn* bremsstrahlung in the SPA. Also, Eq. (2.8) differs from the two-body current contribution derived in Ref. 11 (in the SPA) in the "radial" part, in addition to the extra factor $2/m$. [Unfortunately, in Eqs. (2.14), (2.15a), and (2.17) of Ref. 11, a factor of $1/(2\pi)^3$ is missing. Also, Eqs. (2.15b) and (2.17) of that reference lack a factor e. However, the results presented there remain unchanged, since the correct formulas have been used.] It is a part of this $R_{\rm conv}$ that cancels the two-body contribution.[13]

The rescattering contribution from the magnetization current is given by

$$
\begin{aligned}
R_{\rm magn}=&\left\langle \boldsymbol{\epsilon},\mathbf{k};\phi_{\mathbf{p}'}^{S'M_{S'}}\left|(T^-)^\dagger\frac{1}{E_f}V_{\rm magn}\frac{1}{E_i}T^+\right|0;\phi_{\mathbf{p}}^{SM_S}\right\rangle \\
=&\,i\sqrt{(2\pi)/k}\,\frac{e}{2m}\sum_{M_{S'''},M_{S''''}}\int\frac{d^3p''}{(2\pi)^3}\left[\frac{\mu_1''}{D_-}\left\langle \mathbf{p}'-\frac{\mathbf{k}}{2},-\mathbf{p}'-\frac{\mathbf{k}}{2};S'M_{S'}\left|(T^-)^\dagger\right|\mathbf{p}''-\mathbf{k},-\mathbf{p}'';S'M_{S''}\right\rangle\right. \\
&\left.+\frac{\mu_2''(-)^{S'-S}}{D_+}\left\langle \mathbf{p}'-\frac{\mathbf{k}}{2},-\mathbf{p}'-\frac{\mathbf{k}}{2};S'M_{S'}\left|(T^-)^\dagger\right|\mathbf{p}'',-\mathbf{p}''-\mathbf{k};S'M_{S''}\right\rangle\right] \\
&\times\langle S'M_{S''}|\boldsymbol{\sigma}_1\cdot(\mathbf{k}\wedge\boldsymbol{\epsilon})|SM_{S'''}\rangle\frac{1}{E(p'',p)}\langle \mathbf{p}'';SM_{S'''}|T^+|\mathbf{p};SM_S\rangle\ . \qquad (2.9)
\end{aligned}
$$

Here μ_1'' and μ_2'' are the magnetic moments of the interacting nucleons in units of nuclear magnetons (2.793 for protons and -1.913 for neutrons). In the above equation we have used the fact that

$$
\langle S'M_{S'}|\boldsymbol{\sigma}_2\cdot(\mathbf{k}\wedge\boldsymbol{\epsilon})SM_S\rangle=(-)^{S'-S}\langle S'M_{S'}|\boldsymbol{\sigma}_1\cdot(\mathbf{k}\wedge\boldsymbol{\epsilon})|SM_S\rangle \qquad (2.10)
$$

with $\boldsymbol{\sigma}_1$ and $\boldsymbol{\sigma}_2$ denoting the Pauli spin matrices.

The structure of Eq. (2.9), as far as the momentum integration is concerned, is identical to that of Eq. (2.3) and therefore may be evaluated in the same way as for Eq. (2.3). In the SPA, however, $R_{\rm magn}$ gives no contribution to the bremsstrahlung amplitude because the magnetic current operator is proportional to $\boldsymbol{\sigma}\cdot(\mathbf{k}\wedge\boldsymbol{\epsilon})$. Taking the limit $\mathbf{k}\to 0$, except in that term, Eq. (2.9) reduces to

$$
\begin{aligned}
R_{\rm magn}=&\,i\sqrt{(2\pi)/k}\,\frac{e}{2m}\sum_{M_{S'''},M_{S''''}}\int\frac{d^3p''}{(2\pi)^3}[\mu_1''+(-)^{S'-S}\mu_2'']\langle \mathbf{p}';S'M_{S'}|(T^-)^\dagger|\mathbf{p}'';S'M_{S''}\rangle \\
&\times\left[\frac{\langle S'M_{S''}|\boldsymbol{\sigma}_1\cdot(\mathbf{k}\wedge\boldsymbol{\epsilon})SM_{S''''}\rangle\langle \mathbf{p}'';SM_{S''''}|T^+|\mathbf{p};SM_S\rangle}{E(p'',p')E(p'',p)}\right]\ . \qquad (2.11)
\end{aligned}
$$

It is clear from the above equation that, in this limit, only the initial and final states having the same total spin can contribute to *pp* bremsstrahlung. Using the partial-wave decomposition, Eq. (2.11) yields

$$
\begin{aligned}
R_{\rm magn}=&\sqrt{(2\pi)/k}\,\frac{1}{(2\pi)^3}\sqrt{(4\pi)/3}\,\frac{1}{\pi^2}\left[\frac{e}{m}\right]k[(-)^{S-S'}\mu_1+\mu_2][SS']\begin{Bmatrix}\frac{1}{2} & S' & \frac{1}{2}\\ S & \frac{1}{2} & 1\end{Bmatrix} \\
&\times\sum i^{L-L'}(S'M_{S'}L'M_{L'}|J'M_{J'})(SM_SLM_L|JM_J)[1+(-)^{S'+S+T'+T}] \\
&\times Y_{L'M_{L'}}(\hat{p}')Y_{LM_L}(\hat{p})^*(-)^{L''+M_J}[JJ']\begin{Bmatrix}J & J' & 1\\ S' & S & L''\end{Bmatrix} \\
&\times\sum_{\mu,m_\sigma,m_k}(-)^\mu\epsilon_{-\mu}(JM_JJ'-M_{J'}|1-m_\sigma)(1m_k1m_\sigma|1\mu)Y_{1m_k}(\hat{k}) \\
&\times\int_0^\infty dp''p''^2T_{L''L'}^{J'S'T'}(p'',p')\frac{1}{E(p'',p')E(p'',p)}T_{L''L}^{JST}(p'',p)\ . \qquad (2.12)
\end{aligned}
$$

This completes the derivation of the necessary formulas for calculating the one-body rescattering contribution. Hereafter, we refer to Eqs. (2.11) and (2.12) as the modified soft-photon approximation (MSPA).

III. RESULTS

In the present paper we use the one-boson-exchange potential of Ref. 14 as the bare NN interaction for generating the T matrix. Hereafter, we refer to this potential as one-boson-exchange potential (OBEPQ). Since it does not account for inelasticity, its application is, strictly speaking, restricted to energies below the pion threshold. Nevertheless, in the following subsections, some of the results we present are for energies far beyond the pion threshold (some of them are even beyond the Δ isobar resonance) and, therefore, should be interpreted with caution. In spite of this, we believe those results to be of interest because they give one an idea of how the NN bremsstrahlung cross sections originating from the part of the nuclear Hamiltonian, which describes the elastic processes, behaves at high incident energies. We also call attention to the fact that, in the present formalism, the electromagnetic transition operator is derived from a nonrelativistic nuclear Hamiltonian, and therefore, effects such as relativistic spin corrections are not included which may be considerable,[15,16] especially at high incident and photon energies as we are considering here.

The T-matrix elements in this work are generated as described in Ref. 17, and two-nucleon partial-wave states through $J=11$ are considered. All results shown in the following subsections are calculated in the initial NN c.m. system, except the exclusive cross sections which are in the laboratory frame.

A. *pn* bremsstrahlung

In our previous work,[11] we investigated the pn bremsstrahlung under the conditions appropriate for heavy-ion calculations. In this subsection we further analyze this process paying special attention to the one-body rescattering contribution. However, before discussing these results, we will compare the present calculation with some of the earlier ones in order to check our computer code.

In Fig. 2(a), we show a comparison between the present results and those of Brown and Franklin's[10] for the exclusive bremsstrahlung cross section in the coplanar geometry at an incident energy of $T_{\rm lab}=200$ MeV. Here we use the Hamada-Johnston (HJ) potential for generating the T matrix and the NN partial-wave states through $J=4$ are considered in accordance with Ref. 10. The dashed curve denotes the present result for the external current contribution while the solid one denotes the external plus internal current contributions. The internal current contribution consists of a sum of the one-body rescattering and two-body current contributions. The dotted curves denote the corresponding results of Ref. 10. We see that the present calculation yields results which are close to those of Ref. 10 for both external and external plus internal contributions. We observe, however, a discrepancy of about 10% around the peaks. This discrepancy is disturbing since the formalism and NN potential we use in calculating the bremsstrahlung amplitude are, in principle, the same as those of Ref. 10 (we evaluate this amplitude in momentum space, while in Ref. 10 it is evaluated in coordinate space). The only difference is that, while in Ref. 10 the transformation of coordinates from the initial to final NN c.m. frame is made nonrelativistically, we do this transformation relativistically. In Fig. 2(b), we show the results when the

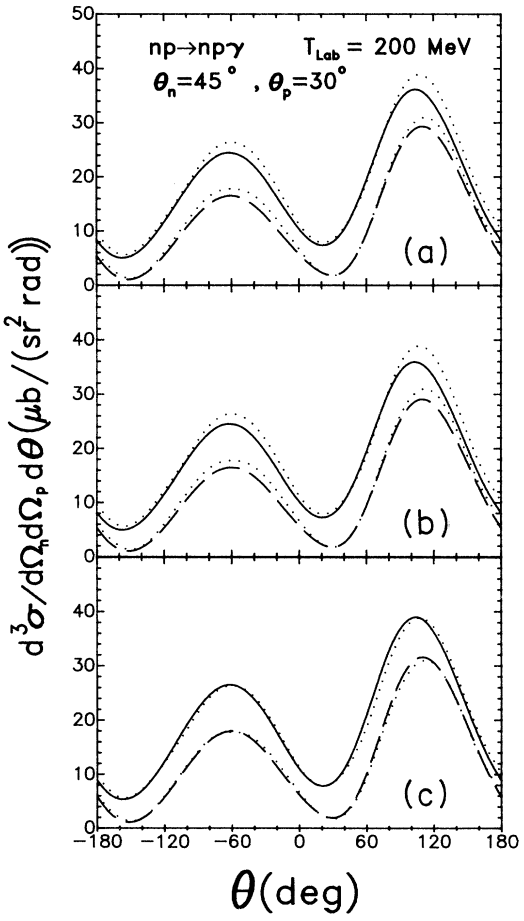

FIG. 2. Coplanar geometry $np\gamma$ cross section in the laboratory frame for neutron incident energy of $T_{\rm lab}=200$ MeV and for nucleon scattering angles of $\theta_n=45°$ and $\theta_p=30°$ as a function of photon emission angle θ. (a) The dashed curve denotes the external current contribution, while the solid one denotes the external plus internal current contributions. The dotted curves are the corresponding results from Ref. 10. The Hamada-Johnston potential is used. The two-nucleon partial-wave states with total spin J up to 4 are included. (b) Same as in (a) but using the nonrelativistic transformation of coordinates from the initial to final NN center-of-mass frame. (c) Same as in (b) but switching off the factor $\sqrt{\varepsilon_{p'}/m}\,\sqrt{\varepsilon_p/m}$ in the invariant transition amplitude (see Appendix B for details).

nonrelativistic transformation is made. Comparing with the results of Fig. 2(a), we see that this has practically no effect on the cross section. This is because, in this geometry where $\theta_n = 45°$ and $\theta_p = 30°$, the photons still have relatively low energies (≤ 43 MeV in the c.m. frame). In Fig. 2(c), we show the results when the factor $\sqrt{m/\varepsilon_{p'}} \rightarrow \sqrt{m/\varepsilon_p}$, which is needed to construct the Lorentz-invariant transition amplitude, is switched off from the T-matrix elements (see Appendix B for remarks). We now see that the agreement between our results and those of Brown and Franklin[10] becomes excellent. We compared our calculations with those of Ref. 10 for other incident energies and nucleon scattering angles and found precisely the same feature as illustrated in Fig. 2. Therefore, the differences between the present results and those of Ref. 10 may be attributed to our inclusion of the above factor.

In Table I the np bremsstrahlung cross section $d^2\sigma/d\Omega_n d\Omega_p$ in the coplanar geometry is shown for several final-state neutron and proton scattering angles. In the third column are the results of Ref. 10 based on the HJ potential, while in the fourth column are the present results also based on the HJ potential. They include all partial-wave states through $J = 4$. We see that our results are smaller than those of Ref. 10 by ~ 10–$20\,\%$ due, basically, to the factor $\sqrt{m/\varepsilon_{p'}}\sqrt{m/\varepsilon_p}$ which is not included in the calculation of Ref. 10 as discussed before. In the fifth column we show the results obtained using the OBEPQ version of the Bonn potential[14] and considering the partial-wave states through $J = 4$. A comparison with the results in the fourth column reveals that the OBEPQ potential yields slightly larger cross sections than the HJ potential. In the sixth and seventh columns are the results based on the OBEPQ potential with the two-nucleon partial-wave states through $J = 6$ and 8, respectively. We see that the inclusion of higher partial-wave states reduces the cross sections considerably as the nucleon scattering angles increase. The results quoted in parentheses are from our previous work[11] where the one-body rescattering contribution was neglected and the NN interaction used there differs from the one used here. Although the experimental data[18] (last column) have large uncertainties, it seems the present calculation still underpredicts the data for large nucleon scattering angles.

Table II shows a comparison between the present calculation and the experimental data of Koehler *et al.*[19] for the $np\gamma$ differential cross section, $d\sigma/d\Omega(\omega_{\rm lab} > 40$ MeV), in the np c.m. frame at an incident energy of $T_{\rm lab} = 197$ MeV for three different photon emission angles θ. The photon energy is integrated from $\omega_{\rm lab} = 40$ MeV. In the last column is the corresponding angle-integrated cross section. The quality of the agreement with the data is similar to that observed for exclusive cross sections. At a lower incident energy of $T_{\rm lab} = 140$ MeV, there is a data point by Edgington and Rose[20] which is

$$\sigma_{\rm tot}(\omega_{\rm lab} > 40 \text{ MeV}) = 4.25 \pm 0.33 \ \mu\text{b} \ .$$

Our calculation yields, for this case, a cross section of 14.5 μb, which is a factor of ~ 3 larger than the measured value, showing a clear incompatibility between the theory and that experiment. However, in view of our prediction at $T_{\rm lab} = 197$ MeV being in reasonable agreement with the data by Koehler *et al.*[19] together with the fact that we believe the $np\gamma$ cross section does not show such a strong incident energy dependence (see discussion of Fig. 5), it may be that the result of Ref. 20 is too small. Indeed, a similar incompatibility was found by Nifenecker *et al.*[21] and Nakayama and Bertsch[22] in the case of proton-nucleus bremsstrahlung.

Having checked our calculations with some of the earlier works and also compared the present results with some of the existing data, we now turn to the discussion of inclusive pn bremsstrahlung processes which are required in heavy-ion calculations.[5,23] Figure 3 illustrates the effect of the rescattering contribution from the one-body current on the double-differential cross section at the photon emission angle of $\theta = 90°$ and incident energies of $T_{\rm lab} = 200$ and 400 MeV. The solid, dashed, dash-dotted, and double-dashed curves correspond to the total, convection, magnetization, and two-body current contributions, respectively, and they include the rescattering term in the SPA [Eq. (2.8)] and MSPA [Eq. (2.12)]. The

TABLE I. The coplanar geometry $np\gamma$ cross section in units of μb/sr^2 in the laboratory frame for an incident energy of $T_{\rm lab} = 200$ MeV. The various neutron and proton scattering angles θ_n and θ_p are in degrees. The present results including the two-nucleon partial-wave states with total spin $J_{\rm max} = 4$, 6, and 8 are in columns denoted by $J \leq 4$, $J \leq 6$, and $J \leq 8$, respectively. They are based on the one-boson-exchange potential from Ref. 14. The results in parentheses under the column denoted by $J \leq 6$ are those from our previous work (Ref. 11). The results of Brown and Franklin (Ref. 10) based on the Hamada-Johnston potential are under the column denoted by HJ(BF). The present results based on the Hamada-Johnston potential are under the column denoted by HJ. The experimental data in the last column are from Ref. 18.

θ_n	θ_p	HJ(BF)	HJ	$J \leq 4$	$J \leq 6$	$J \leq 8$	Expt.
30	30	34.6	30.9	32.1	30.8(34.8)	30.8	35±14
35	35	44.0	38.9	40.1	39.0(43.1)	38.7	57±13
38	38	69.8	56.5	57.6	57.3(64.9)	56.4	116±20
40	30	69.9	58.4	62.7	54.8(58.8)	55.6	114±44
45	30	121.0	107.0	116.0	98.0(94.2)	101.0	132±53

TABLE II. The differential $np\gamma$ cross section $d\sigma/\Omega(\omega_{lab}>40$ MeV) (in units of μb/sr) in the $np\gamma$ center-of-mass frame at an incident neutron energy of $T_{lab}=197$ MeV. The photon emission angle θ is in the $np\gamma$ center-of-mass frame while the photon energy ω_{lab} is in the laboratory system. The last column is the corresponding total cross section in units of μb. Two-nucleon partial-wave states through $J=11$ are included. The experimental data (last row) are from Ref. 19.

$\theta=60°$	$\theta=108°$	$\theta=147°$	$\sigma_{tot}(\omega_{lab}>40$ MeV)
2.6	1.7	0.9	22
3.4±1.0	2.8±0.8	1.8±0.5	35±12

dotted lines are the corresponding results when the rescattering from the one-body current is switched off. One sees that, at $T_{lab}=400$ MeV, this rescattering contribution increases as the photon energy ω approaches its maximum allowed value ω_{max} enhancing the cross section. For the convection part, this term has a minor influence, but for the magnetic part it increases the cross section by a factor of ~ 3 near ω_{max}, so that the magnetization contribution becomes comparable to the two-body contribution. As a result, the one-body rescattering term increases the total contribution by a factor of ~ 1.5 in the region of ω near its end point. Figure 3 also reveals that this enhancement of the cross section is confined to the region of ω close to its maximum. The crosses in Fig. 3 refer to the corresponding results with the full rescattering contribution [Eqs. (2.3) and (2.9)]. These show that, in calculating inclusive cross sections, the SPA and MSPA for the one-body rescattering term are excellent, even for very high-energy photons. At $T_{lab}=200$ MeV, the effect of the one-body rescattering term is very small over the full range of photon energies.

Figure 4 shows the effect of the one-body rescattering contribution on the angular distribution at $\omega=75$ and 150 MeV and for $T_{lab}=200$ and 400 MeV, respectively. As can be seen, the one-body rescattering contribution enhances the cross section for forward and backward photon emission angles. Of course, the size of this enhancement depends strongly on the photon energy considered, as we have seen in Fig. 3. Again we see that the SPA and MSPA for the rescattering are excellent. We also see that the two-body current contribution is nearly isotropic. Figure 4, therefore, shows that the internal

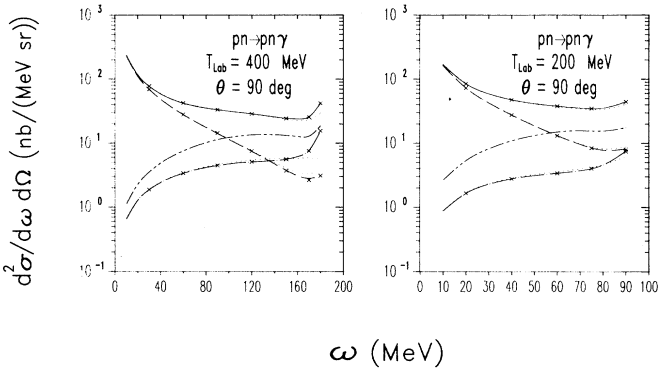

FIG. 3. Effect of the one-body rescattering contribution on the double-differential $pn\gamma$ cross section in the initial proton-neutron center-of-mass frame as a function of the photon energy ω and at the photon emission angle $\theta=90°$. The incident energies are, from right to left, $T_{lab}=200$ and 400 MeV. The dash-dotted, dashed, double-dashed, and the solid curves denote the contributions from the magnetization, convection, two-body, and total current contributions, respectively. The convection and magnetization parts include the rescattering term in the SPA [Eq. (2.8)] and MSPA [Eq. (2.12)]. The dotted lines are the corresponding results when the rescattering from the one-body current is switched off. The crosses refer to the results with the full rescattering contribution [Eqs. (2.3) and (2.9)]. The OBEPQ version of the Bonn potential (Ref. 14) is used. Two-nucleon partial-wave states through $J=11$ are included.

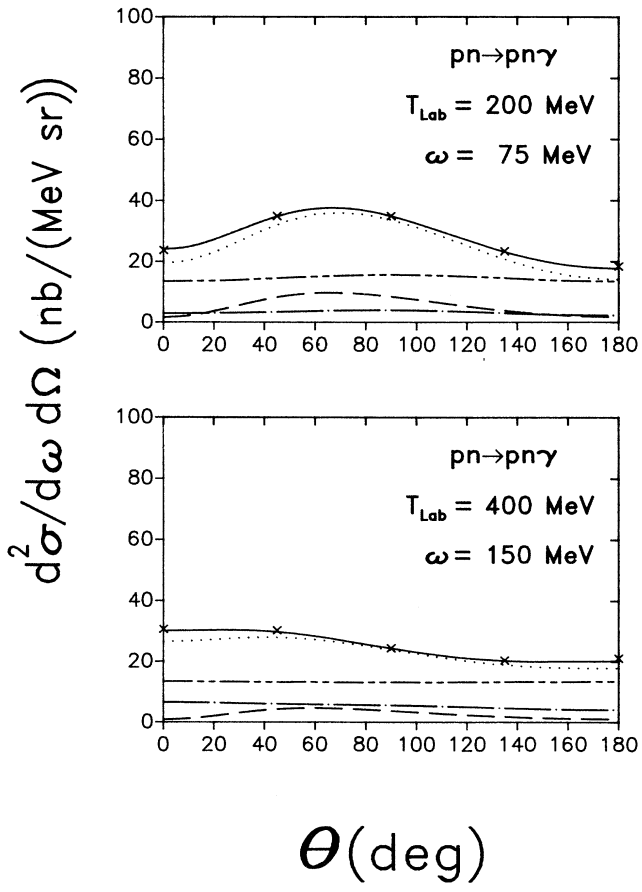

FIG. 4. Effect of the one-body rescattering contribution on the angular distribution for the $pn\gamma$ process calculated in the initial neutron-proton center-of-mass frame. The upper part corresponds to the incident energy $T_{lab}=200$ MeV and the photon energy $\omega=75$ MeV, while the lower one corresponds to $T_{lab}=400$ MeV and $\omega=150$ MeV. For further details see the caption of Fig. 3.

current contribution (rescattering from the one-body current plus two-body current) gives roughly an isotropic angular distribution.

Hereafter, in this subsection, the one-body rescattering term will be calculated in the SPA and MSPA for the convection and magnetization current contributions, respectively. In Fig. 5 we show the double-differential cross section as a function of photon energy at $\theta=30°$ for $T_{\rm lab}=150$, 300, and 600 MeV. The contributions arising from the different parts of the current are shown separately. We see that they show very similar features. The cross section (total contribution) drops basically as $1/\omega$ in the low photon energy region, which is governed by the convection current contribution, and then stays rather constant due to the increasing contribution from the two-body and magnetization currents. The latter has a linear dependence on ω in the low-energy region [see Eq. (3.2)]. The behavior of the two-body contribution can be understood if we consider the one-pion-exchange current contribution as discussed in Ref. 11. As the photon energy approaches its end point, the cross section increases rapidly. This feature has been also noticed and discussed in our previous work.[11] The incident energy dependence of the photon cross section is determined by the incident energy dependence of the T matrix and of the electromagnetic current operator, as well as by the energy denominator in the intermediate states. The np T matrix has a rather strong energy dependence up to $T_{\rm lab}\sim 200$ MeV. This is a consequence of the strong energy dependence of np total cross section σ_{np} which drops as the incident energy increases. The convection current operator also contains an incident energy dependence since it comes from the kinetic-energy part of the nuclear Hamiltonian, while the magnetization current operator has no such dependence [apart from momentum-conserving δ function (see Ref. 11)] because it is related to the magnetic moment of the nucleon. In Fig. 5 we observe that, in the region of the incident energy considered and for a given photon energy, the convection current contribution increases as the incident energy increases (note the difference in the scale in Fig. 5). This can be understood since the incident energy dependence of the convection current contribution is contained in the factor $T_{\rm lab}\sigma_{np}(T_{\rm lab})$ in the SPA [see Eq. (3.1)]. The np total cross section $\sigma_{np}(T_{\rm lab})$ does not drop as fast as $1/T_{\rm lab}$ in the region of incident energy considered. For lower incident energies, the $pn\gamma$ cross section can decrease as a function of incident energy. The magnetic contribution is rather insensitive to the incident energy; in this case the energy dependence of the np T matrix counterbalances that of the energy denominator. The two-body contribution decreases as a function of incident energy for a fixed ω; the current operator here depends on momentum transfer rather than on relative momentum.[11] As a consequence of these behaviors, the total contribution depends rather weakly on the incident energy, except in the low photon energy region where it is entirely dominated by the convection contribution.

In Figs. 6(a), (b), and (c) the angular distributions for various photon energies ω are shown at $T_{\rm lab}=150$, 300, and 600 MeV, respectively. For low incident energies, the shape of the angular distribution is dictated by the convection current even for relatively high ω as illustrated in Fig. 6(a). Note that the two-body and magnetization currents yield nearly isotropic angular distributions. At $T_{\rm lab}=300$ MeV [see Fig. 6(b)], the situation is still very similar to what we see at lower incident energies, except that the angular distribution is much more pronounced at low photon energies due to the relatively larger contribution of the convection current. However, at higher ω [see the upper part of Fig. 6(b)], the angular distribution is much less pronounced because of the suppression of the convection current. A remarkable change in the shape of the angular distribution as a function of photon energy can be observed at much higher incident energies as illustrated in Fig. 6(c). We see that the

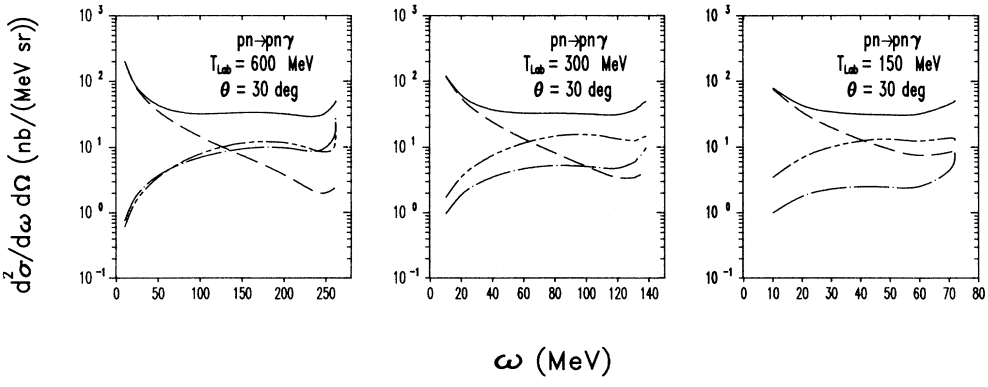

FIG. 5. $pn\gamma$ cross section in the initial neutron-proton center-of-mass frame as a function of photon energy ω at the photon emission angle of $\theta=30°$. The incident energies are, from right to left, $T_{\rm lab}=150$, 300, and 600 MeV. For further details see the caption of Fig. 3.

shape changes from a roughly $\sin^2\theta$ to a $\cos^2\theta$ dependence as the photon energy increases from $\omega=30$ to 230 MeV.

The general feature of the angular distribution can be understood by examining the contribution arising from the external current (one-body current excluding the rescattering). To this end let us consider the bremsstrahlung amplitude from the one-body external current as given by Eqs. (3.8) and (3.9) in Sec. III C. Then, following Ref. 11, the individual $pn\gamma$ cross sections to leading order are

$$\frac{d^2\sigma_{\rm conv}}{d\omega\, d\Omega}=\frac{\alpha}{(2\pi)^2}\frac{1}{\omega}\left[\frac{p'}{p}\right]\left[\frac{\varepsilon(p')\varepsilon(p)T_{np}^2}{4\pi}\right]\times(\tfrac{2}{3}v'^2+v^2\sin^2\theta) \tag{3.1}$$

for the convection current contribution and

$$\frac{d^2\sigma_{\rm magn}}{d\omega\, d\Omega}=\frac{1}{2}\frac{\alpha}{(2\pi)^2}\frac{\omega}{m^2}\left[\frac{p'}{p}\right]\times\left[\frac{\varepsilon(p')\varepsilon(p)T_{np}^2}{4\pi}\right](\mu_p^2+\mu_n^2)\times\left[[(g-d)^2+\tfrac{1}{3}g^2v'^2]+d^2v^2\cos^2\theta-2d(g-d)\frac{\mu_p^2-\mu_n^2}{\mu_p^2+\mu_n^2}v\cos\theta\right] \tag{3.2}$$

for the magnetic contribution. Here $\alpha=e^2$ is the fine-structure constant, and the subscripts n and p stand for

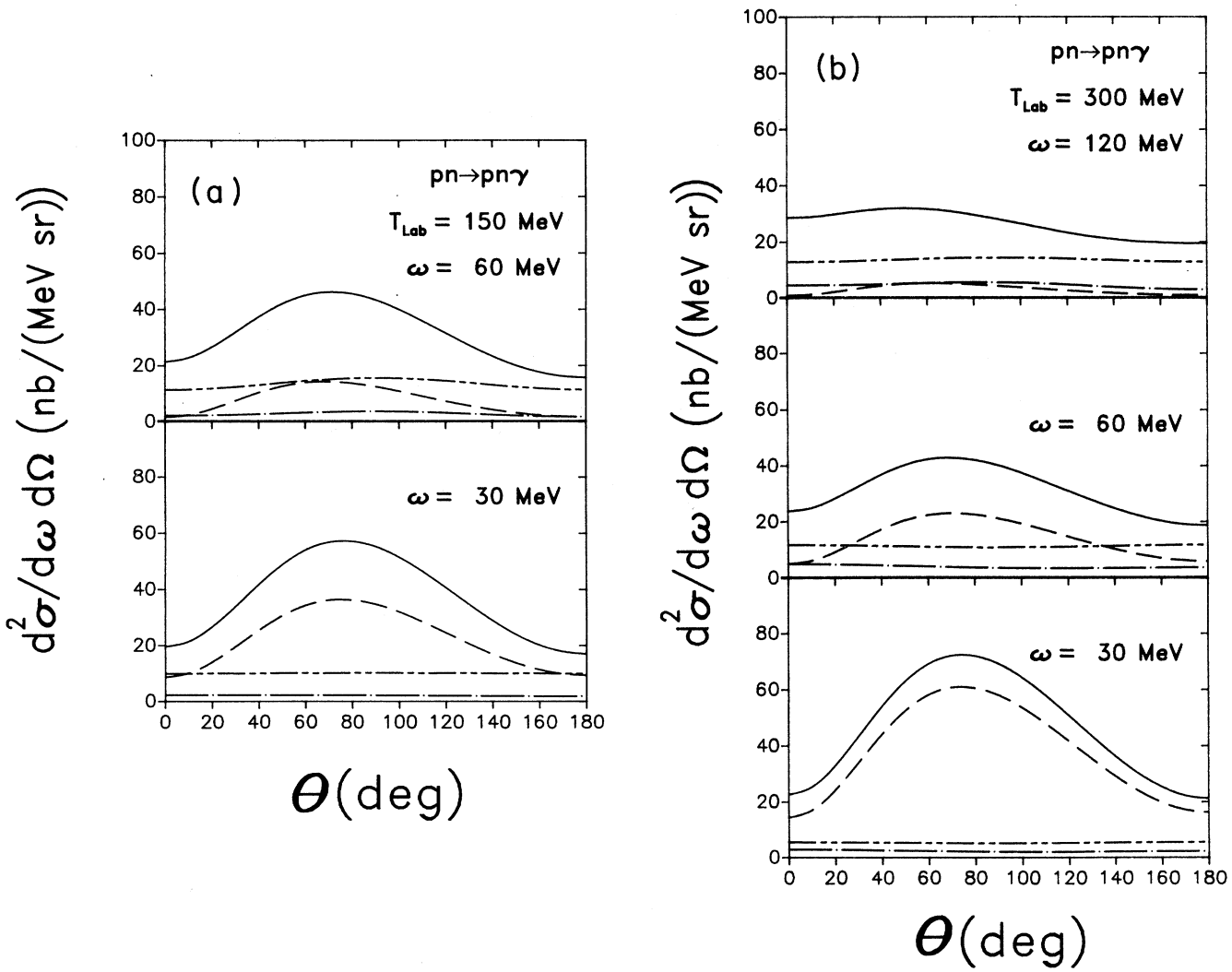

FIG. 6. $pn\gamma$ angular distribution in the initial neutron-proton center-of-mass-frame. (a) corresponds to an incident energy of $T_{\rm lab}=150$ MeV and photon energies of $\omega=30$ and 60 MeV (lower and upper part, respectively). (b) is at $T_{\rm lab}=300$ MeV for photon energies of $\omega=30$, 60, and 120 MeV (lower, middle, and upper parts, respectively). (c) corresponds to an incident energy of $T_{\rm lab}=600$ MeV and photon energies of, from bottom to top, $\omega=30$, 60, 120, and 230 MeV. For further details, see the caption of Fig. 3.

neutron and proton, respectively. We have also omitted explicit reference to the arguments of T_{np}, d, and g. The quantity in the large parentheses in Eqs. (3.1) and (3.2) becomes the total np cross section σ_{np} in the SPA limit. The classical bremsstrahlung formula may be recovered from Eq. (3.1) if we drop there the phase-space factor (p'/p) and replace the quantity in the large parentheses by σ_{np}.

We first concentrate on the convection part. Equation (3.1) shows that the angular distribution from that contri-

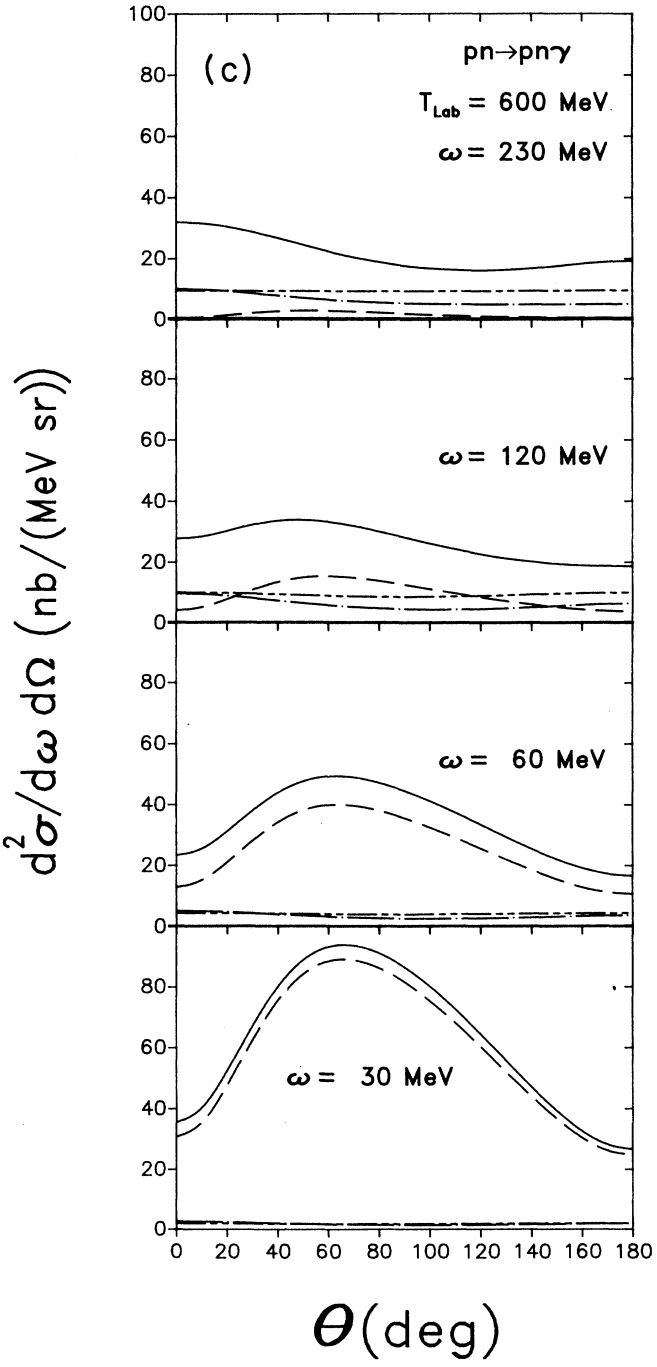

FIG. 6. (*Continued*).

bution has the well-known dipole shape. Moreover, it becomes more pronounced as the incident energy increases because of the factor v^2, which is approximately proportional to $T_{\rm lab}$. The photon cross section also goes basically as $1/\omega$. These features are what we observe qualitatively in Fig. 6. The small asymmetry around $\theta=90°$ in Fig. 6 is due to the higher-order correction in the bremsstrahlung amplitude which has been neglected in Eq. (3.1). Also, the deviation from a $1/\omega$ dependence in the high photon energy region, as can be observed better in Fig. 5, is mainly due to the energy dependence of the T matrix. We observe that, for high-energy photons, the effective incident energy is small.

The magnetic contribution yields a combination of terms linear and quadratic in $\cos\theta$ in addition to a term independent of the photon emission angle. However, the value of the parameters d and g (see Table III) are such that the term independent of the photon angle gives the dominant contribution, followed by the $\cos^2\theta$ term. The term linear in $\cos\theta$ is suppressed to a large extent. For example, at $T_{\rm lab}=300$ MeV, using the values of d and g quoted in Table III, the $pn\gamma$ cross-section angular dependence is given by

$$\frac{d^2\sigma_{\rm magn}}{d\omega\, d\Omega}(T_{\rm lab}=300\ \text{MeV}) \propto \left[\left(\frac{1.20}{v'^2}+\frac{0.17}{3} \right) v'^2 + 2.27 v^2\cos^2\theta + 0.90 \left(\frac{\mu_p^2-\mu_n^2}{\mu_p^2+\mu_n^2} \right) v\cos\theta \right] . \tag{3.3}$$

TABLE III. Fitted parameters a, b, a', and b' (third, fourth, seventh, and eighth columns, respectively) in Eq. (3.11) and for g and d (fifth and sixth columns, respectively) in Eq. (3.9). The first column is the nucleon incident energy $T_{\rm lab}$ in the laboratory frame, while the second column is the corresponding value in the nucleon-nucleon center-of-mass frame.

$T_{\rm lab}$ (MeV)	$E_{\rm c.m.}$ (MeV)	a (MeV fm^3)	b (MeV^{-1})	g	d	a' (MeV fm^3)	b' (MeV^{-1})
10.0	4.99	−1356.2	9.59×10^{-2}	0.687	1.643	0.992	1.02×10^{-1}
15.0	7.49	−1150.2	7.30×10^{-2}	0.679	1.641	0.988	7.61×10^{-2}
25.0	12.46	−849.5	5.41×10^{-2}	0.654	1.636	0.980	4.39×10^{-2}
50.0	24.84	−543.5	3.57×10^{-2}	0.622	1.624	0.960	2.12×10^{-2}
75.0	37.13	−434.6	2.12×10^{-2}	0.585	1.612	0.941	1.37×10^{-2}
100.0	49.35	−369.1	1.48×10^{-2}	0.560	1.600	0.922	1.10×10^{-2}
125.0	61.50	−325.4	1.24×10^{-2}	0.532	1.588	0.904	9.30×10^{-3}
150.0	73.56	−301.9	9.64×10^{-3}	0.505	1.576	0.886	7.92×10^{-3}
175.0	85.55	−285.1	7.86×10^{-3}	0.485	1.564	0.869	7.07×10^{-3}
200.0	97.47	−272.8	6.41×10^{-3}	0.468	1.553	0.852	6.52×10^{-3}
225.0	109.32	−265.3	5.09×10^{-3}	0.452	1.541	0.836	6.00×10^{-3}
250.0	121.10	−257.2	4.35×10^{-3}	0.436	1.530	0.820	5.52×10^{-3}
275.0	132.80	−250.1	3.62×10^{-3}	0.423	1.518	0.804	5.23×10^{-3}
300.0	144.44	−243.5	3.12×10^{-3}	0.410	1.507	0.789	4.93×10^{-3}
325.0	156.02	−238.1	2.96×10^{-3}	0.395	1.496	0.774	4.63×10^{-3}
350.0	167.53	−233.0	2.73×10^{-3}	0.380	1.484	0.760	4.44×10^{-3}
375.0	178.97	−228.1	2.68×10^{-3}	0.369	1.473	0.746	4.21×10^{-3}
400.0	190.35	−222.8	2.53×10^{-3}	0.357	1.462	0.732	4.05×10^{-3}
425.0	201.67	−217.9	2.40×10^{-3}	0.345	1.451	0.718	3.91×10^{-3}
450.0	212.93	−214.1	2.27×10^{-3}	0.332	1.441	0.705	3.70×10^{-3}
475.0	224.13	−209.0	2.20×10^{-3}	0.322	1.430	0.692	3.63×10^{-3}
500.0	235.26	−205.0	2.09×10^{-3}	0.311	1.419	0.680	3.50×10^{-3}
525.0	246.34	−201.7	2.02×10^{-3}	0.301	1.408	0.668	3.41×10^{-3}
550.0	257.37	−197.5	1.97×10^{-3}	0.290	1.398	0.656	3.32×10^{-3}
575.0	268.33	−194.1	1.93×10^{-3}	0.280	1.387	0.644	3.26×10^{-3}
600.0	279.24	−190.7	1.83×10^{-3}	0.270	1.377	0.633	3.10×10^{-3}
625.0	290.09	−187.7	1.80×10^{-3}	0.256	1.367	0.621	3.03×10^{-3}
650.0	300.90	−185.0	1.70×10^{-3}	0.242	1.357	0.611	2.89×10^{-3}
675.0	311.64	−182.0	1.62×10^{-3}	0.234	1.346	0.600	2.76×10^{-3}
700.0	322.34	−179.2	1.49×10^{-3}	0.225	1.336	0.589	2.64×10^{-3}
725.0	332.98	−176.9	1.43×10^{-3}	0.213	1.326	0.579	2.55×10^{-3}
750.0	343.57	−174.0	1.39×10^{-3}	0.200	1.319	0.569	2.48×10^{-3}
775.0	354.11	−171.7	1.33×10^{-3}	0.188	1.314	0.560	2.42×10^{-3}
800.0	364.61	−169.1	1.30×10^{-3}	0.175	1.310	0.550	2.41×10^{-3}

Since $v' < v$ and $v^2 = 0.14$ at this incident energy, we see that the ratio between the θ independent and $\cos^2\theta$ terms is at least 4. This should be contrasted to the corresponding ratio of $\frac{2}{3}$ for the convection current contribution [see Eq. (3.1)]. The angular distribution from the magnetization current is, therefore, much less structured than the convection current contribution. It is interesting to note that the dominant term in Eq. (3.2) is also independent of v'^2. The term linear in $\cos\theta$ introduces a small asymmetry in the angular distribution around $\theta = 90°$ which is difficult to see in Fig. 6 at that scale. Equation (3.2) also shows that the angular distribution becomes more pronounced as a function of incident energy. The deviation from Eq. (3.2) observed in Fig. 6 is basically due to the spin-projection diagonal approximation of the T matrix made in Eq. (3.9). For example, the angular distribution in Fig. 6 at $T_{\rm lab} = 150$ and 300 MeV and for high photon energies shows a slight enhancement around $\theta = 90°$. This is caused by the strong off-diagonal $^3(SD)_1$ and diagonal $^3D_1$ tensor states which make the spin-projection diagonal approximation of the T matrix less accurate. However, we see that, at these incident energies, the magnetic contribution still plays a relatively minor role as far as the shape of the angular distribution is concerned. At much higher incident energies, where a very high photon energy region can be reached [see Fig. 6(c)], the magnetic contribution shows a $\cos^2\theta$ dependence, in accordance with the approximate formula given by Eq. (3.2). In any case, the qualitative features of the angular distribution where the magnetization current becomes really important can be understood from Eq. (3.2) which also shows that the cross section has a linear dependence on the photon energy. The deviation from this dependence in the high-energy region is due, largely, to the energy dependence of the T matrix. A comparison of Eqs. (3.1) and (3.2) shows that the small contribution of the magnetization current with respect to the convection current is due to the smallness of the nucleon magnetic moment, which is proportional to the inverse of nucleon mass m. This is reflected in the factor $1/m^2$ in Eq. (3.2).

As a result of the behavior of the convection and magnetization current contributions, the total contribution exhibits the angular distribution shown in Fig. 6. We again observe that the internal current yields basically an isotropic angular distribution.

Before leaving this subsection we shall discuss the important question of gauge invariance. In order to preserve the gauge invariance of the theory, each contribution from different parts of the internal current should be treated in the same order of perturbation.[13] In Figs. 3 and 4 we have shown that the rescattering contribution from the one-body current increases the photon cross section considerably in the photon energy region near its end point, due essentially to the magnetic current. As mentioned in Sec. II, this gives a nonvanishing contribution only beyond the SPA. On the other hand, the two-body current contribution is considered only in the SPA (the minimal substitution alone is insufficient to obtain uniquely the electromagnetically induced two-body potential beyond the SPA). Therefore, the gauge invariance is violated if we include the one-body rescattering contribution beyond the SPA and the two-body contribution in the SPA, as in the present work. However, in Ref. 11 we have estimated that the SPA for the two-body current is a good approximation as far as the inclusive cross sections are concerned. In view of this fact, we believe the violation of the gauge invariance in the present case is not as critical as it might appear at first.

B. *pp* bremsstrahlung

In this subsection we analyze the *pp* bremsstrahlung. This process is usually ignored in calculations where the $pn\gamma$ process is also present. The latter gives rise to dipole radiation while the $pp\gamma$ process yields quadrupole radiation in the SPA. However, the ratio of *pp* to *pn* bremsstrahlung cross sections is certainly larger when high-energy photons are produced than for soft-photon production; recall that the convection current contribution drops as the photon energy increases, while the magnetic contribution increases with photon energy. The main purpose of this subsection is, therefore, to investigate the relevance of the $pp\gamma$ process with respect to the $pn\gamma$ process in producing energetic photons.

In the present work we neglect the influence of the Coulomb interaction. We also recall that all the formulas derived in Ref. 11 and in the previous section apply for both *pn* and *pp* bremsstrahlung. The relevant differences in both cases are the normalization factors of the wave functions in terms of isospin states and the integration only over half the *pp* final-state solid angle in the $pp\gamma$ process.

As in the case of the *pn* bremsstrahlung, we first compare the present calculation with some of the earlier ones. In Figs. 7(a) and (d) we show a comparison between our results and those by Brown[24] for the exclusive $pp\gamma$ cross section in the coplanar geometry at an incident energy of $T_{\rm lab} = 158$ MeV. Here we use the HJ potential. Also, the two-nucleon partial-wave states through $J = 4$ are considered for purposes of comparison with Ref. 24. Figure 7(a) shows the results from the external current contribution, while Fig. 7(d) shows the results from the external plus internal current contributions. The solid curves denote the present calculation and the dotted ones are the results of Ref. 24. We find excellent agreement between the two calculations. However, this excellent agreement is accidental. Figures 7(b) and (e) show the same comparison as in Figs. 7(a) and (d), respectively, but with our results obtained using the nonrelativistic transformation of coordinates from the initial to final *NN* c.m. frame, as was used in Ref. 24. In contrast to the results of Fig. 2, here we see that this has a non-negligible effect on the cross section and that the agreement between the two calculations deteriorates. We note that the relevance of the relativistic transformation of coordinates from the initial to final *NN* c.m. frame is determined not only by the momentum of the emitted photon but also by how strongly the T matrix varies with the relative momenta of the nucleons. In fact, in the case of Fig. 7, the energy of the photon is ≤ 55 MeV in the c.m. system, only about 10 MeV larger than in the case of Fig. 2. However, here the T matrix has much stronger momentum dependence than

in the case of Fig. 2, and its magnitude is also larger, since we probe the lower effective incident energy region. Therefore, a relatively small difference in the values of momenta of nucleons will affect the results. We also note that, for some special cases, the relativistic transformation of coordinates from the initial to final NN c.m. frame changes the results by $\sim 10\%$ even for incident energy as low as $T_{\rm lab}=100$ MeV. In Figs. 7(c) and (f), we show the same comparison as in Figs. 7(b) and (e), respectively, when the factor $\sqrt{m/\varepsilon_{p'}}\sqrt{m/\varepsilon_p}$ in the T-matrix elements (see Appendix B for the details) in our results is switched off. Again we find excellent agreement between the two calculations. We have compared our results with those by Brown[24] for other incident energies and proton scattering angles and found the same feature as illustrated in Figs. 7(b), (c), (e), and (f).

In Fig. 8 we show a comparison between the present results and those by Drechsel and Maximon[25] for the exclusive $pp\gamma$ cross section in the coplanar geometry at low incident energies of $T_{\rm lab}=30$ MeV [Fig. 8(a)] and $T_{\rm lab}=10$ MeV [Fig. 8(b)]. We use the HJ potential as in Ref. 25. The solid curves are the present results, while the dashed ones correspond to those of Ref. 25. We see that the two calculations are in very good agreement.

Figure 9 shows a comparison between the results based on the HJ (solid line) and the OBEPQ (dash-dotted line)

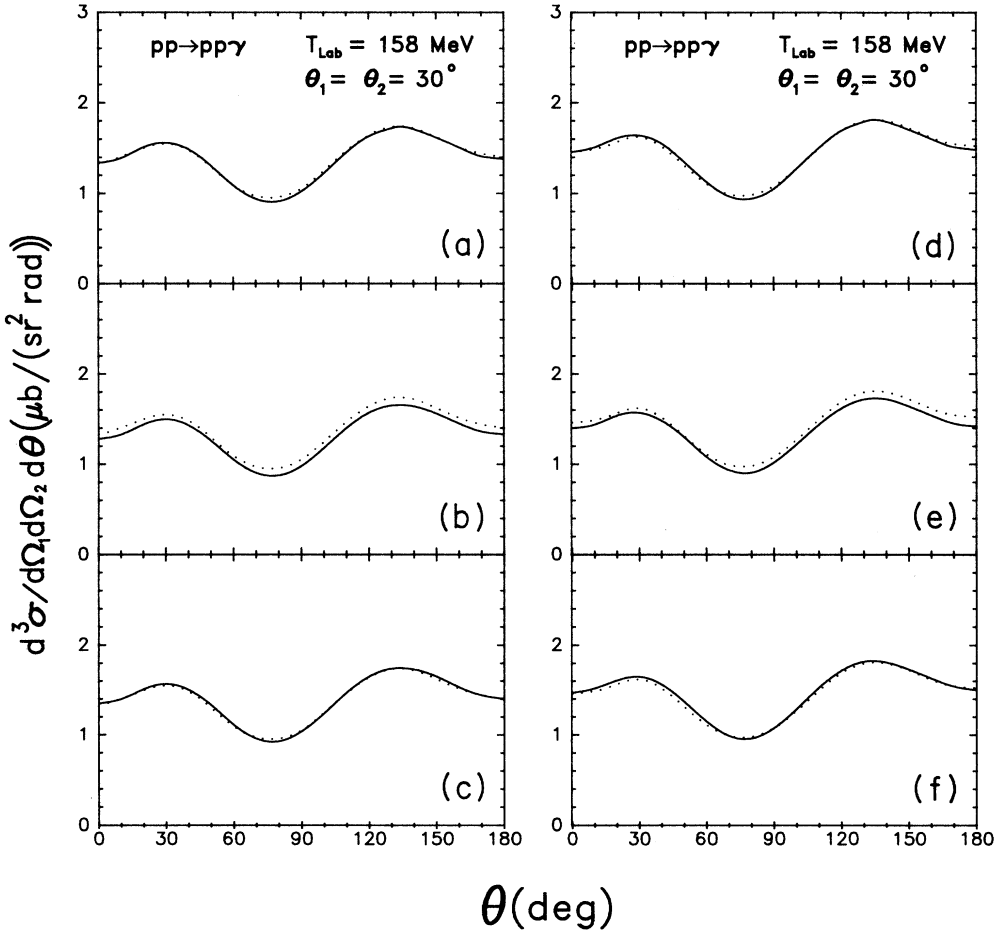

FIG. 7. Coplanar geometry $pp\gamma$ cross section in the laboratory frame for incident energy $T_{\rm lab}=158$ MeV and for proton scattering angles $\theta_1=\theta_2=30°$ as a function of photon emission angle θ. The left-hand side are the results from the external current contribution, while the right-hand side are from the external plus internal current contributions. The solid curves in (a) and (d) are the present results based on the Hamada-Johnston potential with partial-wave states $J\leq 4$. The dotted curves are the corresponding results from Ref. 24. (b) and (e) are the same as (a) and (d), respectively, but using the nonrelativistic transformation of coordinates from the initial to final nucleon-nucleon center-of-mass frame in the present calculation. (c) and (f) are the same as (b) and (e), respectively, but switching off the factor $\sqrt{m/\varepsilon_{p'}}\sqrt{m/\varepsilon_p}$ in the T-matrix elements (see Appendix B for the details) in the present calculation.

potentials for the exclusive $pp\gamma$ cross section at $T_{lab}=158$ MeV together with the experimental data.[26] The OBEPQ potential yields a cross section which is shifted upwards by ~ 0.3 μb/sr^2 rad with respect to that based on the HJ potential. The quality of the agreement with the data seems to be slightly better in the case of the OBEPQ than the HJ potential. However, within the uncertainties in the experimental data, it is not possible to discard any of these potentials.

In Fig. 10, a comparison between the results based on the HJ (solid curve) and the OBEPQ (dash-dotted curve) potentials is made together with the experimental data[27] for a lower incident energy of $T_{lab}=42$ MeV. We see again that the OBEPQ potential yields larger cross sections than the HJ potential. Here, the HJ potential gives better agreement with the data. The dotted curve in Fig. 10 corresponds to the result of Ref. 28 in the soft-photon approximation.

From what we have discussed so far, the OBEPQ version of the Bonn potential[14] seems to yield cross sections which are systematically larger than those based on the HJ potential. However, this feature depends on the region of the incident energy we are considering. To illustrate this we show results in Fig. 11 for the $pp\gamma$ cross sections in the coplanar geometry at an incident energy of $T_{lab}=200$ MeV. We see that the two potentials yield, for this case, results which are much closer to each other than at lower incident energies. Moreover, in this case,

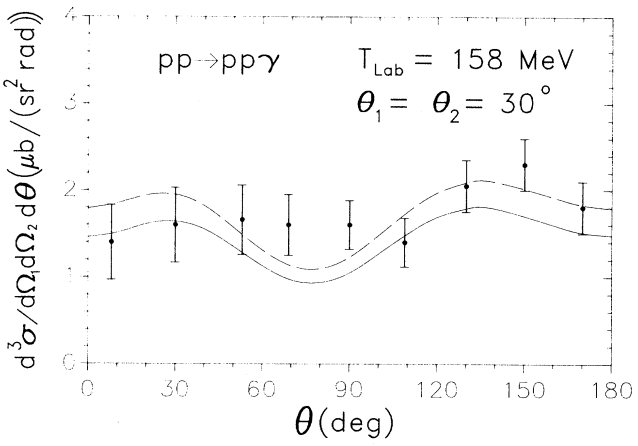

FIG. 9. Coplanar geometry $pp\gamma$ cross section in the laboratory frame for incident energy $T_{lab}=158$ MeV and for proton scattering angles $\theta_1=\theta_2=30°$ as a function of photon emission angle θ. The solid curve denotes the result based on the HJ potential, while the dash-dotted curve corresponds to that based on the OBEPQ potential (Ref. 14). Two-nucleon partial-wave states through $J=4$ are included. The data are from Ref. 26.

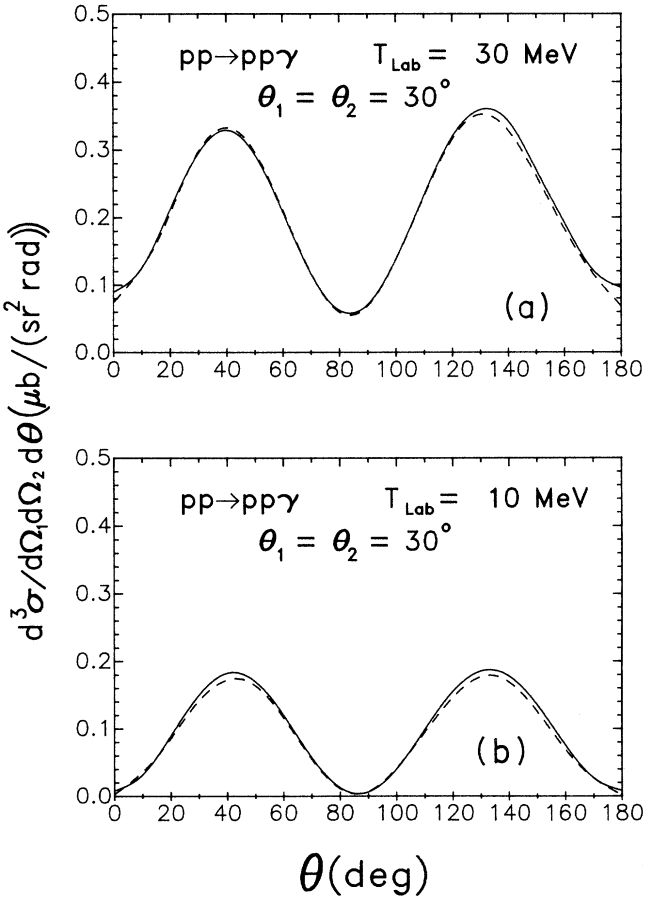

FIG. 8. $pp\gamma$ exclusive cross section in the coplanar geometry at incident energies of (a) $T_{lab}=30$ MeV and (b) $T_{lab}=10$ MeV. The proton scattering angles are $\theta_1=\theta_2=30°$. The solid curves denote the present results, while the dashed ones correspond to those from Ref. 25. The Hamada-Johnston potential is used with all partial-wave states with $J\leq 4$.

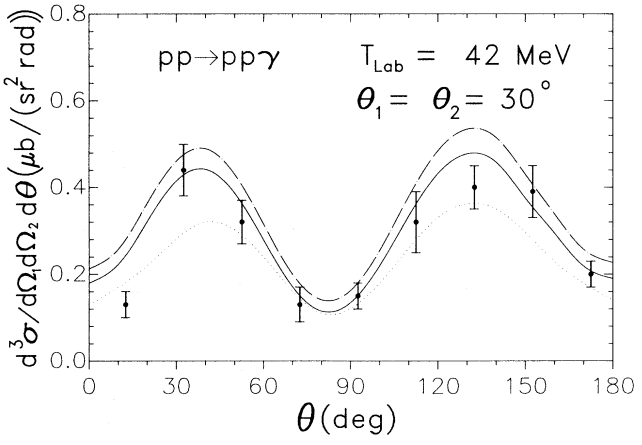

FIG. 10. $pp\gamma$ cross section in the same geometry as in Fig. 9 but for an incident energy $T_{lab}=42$ MeV. The solid line is the result based on the HJ potential, while the dash-dotted line corresponds to that from the OBEPQ potential (Ref. 14). All partial-wave states through $J=4$ are considered. The dotted line is the soft-photon approximation result of Ref. 28. The data are from Ref. 27.

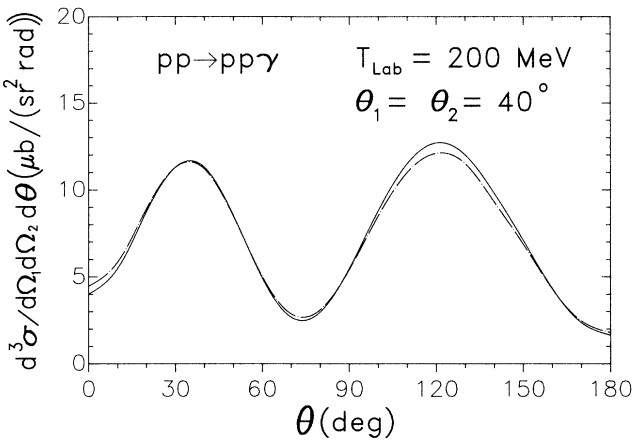

FIG. 11. Coplanar geometry $pp\gamma$ cross section in the laboratory frame for an incident energy $T_{\rm lab}=200$ MeV and for proton scattering angles $\theta_1=\theta_2=40°$ as a function of photon emission angle θ. The solid line is the result based on the HJ potential, while the dash-dotted curve corresponds to that based on the OBEPQ potential (Ref. 14). Two-nucleon partial-wave states through $J=4$ are included.

the cross section based on the OBEPQ potential (dash-dotted curve) is smaller than that based on the HJ potential (solid curve) around $\theta=130°$. A more detailed analysis of the exclusive bremsstrahlung processes will be presented in a future work.

We now discuss results for $pp\gamma$ inclusive cross sections which are more appropriate for heavy-ion calculations. In Fig. 12(a) the effect of the one-body rescattering contribution is shown. As in the $pn\gamma$ process in Fig. 3, the solid, dashed, and dash-dotted curves correspond to the total, convection, and magnetization current contributions, respectively, with the rescattering term included in the SPA [Eq. (2.8)] and MSPA [Eq. (2.12)]. The crosses are the results with the full rescattering [Eqs. (2.3) and (2.9)]. The dotted lines are the corresponding results without the rescattering. We observe that in the SPA there is neither a one-body rescattering term nor a two-body contribution to the pp bremsstrahlung. First, we see in Fig. 12(a) that the inclusion of the one-body rescattering term (crosses) enhances the cross section in the high photon energy region, similar to what we have seen in Fig. 5 for pn bremsstrahlung. However, since the two-body current is absent in this case, the rescattering effect on the total contribution is very large compared to the $pn\gamma$ process for ω near its maximum. We also see that the SPA and MSPA for the rescattering correction are good approximations, except for ω very close to its end point, where the MSPA largely underestimates the cross section. Figure 12(b) illustrates the one-body rescattering effect on the angular distribution. As can be seen, it essentially enhances the photon cross section for forward and backward photon angles as in the case of the $pn\gamma$ process. The MSPA for the rescattering provides a good description of the shape of the angular distribution calculated exactly.

Although the MSPA for the rescattering underestimates the $pp\gamma$ cross section for photon energies very close to $\omega_{\rm max}$ as we have seen in Fig. 12(a), hereafter in this subsection we include its contribution only in this limit. This, however, does not spoil the following analysis.

In Fig. 13 the differential photon cross sections as a function of ω are shown for $T_{\rm lab}=150$, 300, and 600 MeV, and at the photon emission angle of $\theta=30°$. In the

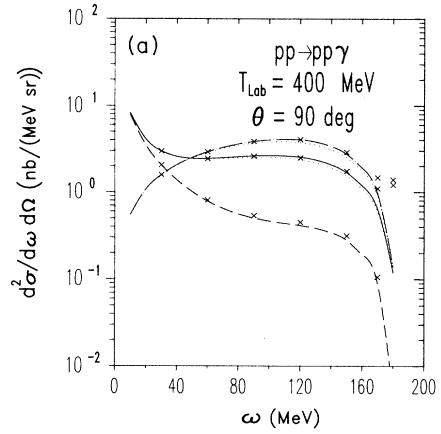

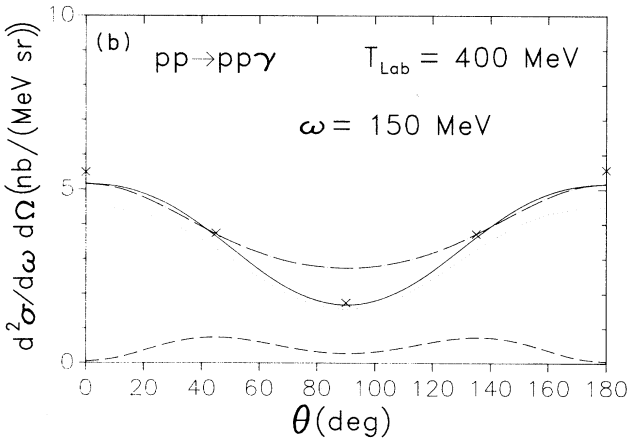

FIG. 12. (a) Effect of the one-body rescattering contribution on the double-differential $pp\gamma$ cross section in the initial proton-proton center-of-mass frame as a function of the photon energy ω at the photon emission angle $\theta=90°$. The incident energy is $T_{\rm lab}=400$ MeV. The solid, dashed, and dash-dotted curves correspond to the total, convection, and magnetic current contributions, respectively, and included the rescattering term in the SPA [Eq. (2.8)] and MSPA [Eq. (2.12)]. The dotted lines are the corresponding results when the rescattering contribution is switched off. The crosses refer to the results with the full rescattering contribution [Eqs. (2.3) and (2.9)]. The OBEPQ potential (Ref. 14) is used including all partial-wave states through $J=11$. (b) Effect of the one-body rescattering contribution on the angular distribution for the $pp\gamma$ process in the initial proton-proton center-of-mass frame. The incident energy is $T_{\rm lab}=400$ MeV and the photon energy is $\omega=150$ MeV. For further details see (a).

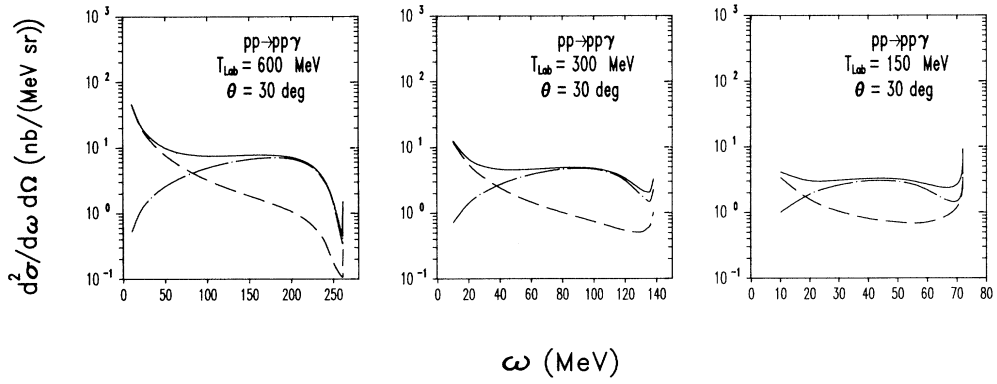

FIG. 13. $pp\gamma$ cross section in the initial proton-proton center-of-mass frame, as a function of photon energy ω at the photon emission angle $\theta=30°$. The incident energies are (from right to left) $T_{\rm lab}=150$, 300, and 600 MeV. For further details see the caption of Fig. 12(a).

low-ω region, the cross section (total contribution) falls as $1/\omega$ and is dominated by the convection current contribution. Then, as the photon energy increases, the cross section remains rather constant because of the increasing magnetic contribution. These features are very similar to those of pn bremsstrahlung (see Fig. 5). As the photon energy becomes larger, the cross section starts to drop. This is not observed in the $pn\gamma$ process because of the two-body contribution, which is absent here. At the end point the photon cross section increases rapidly, as in the case of $pn\gamma$. Recall that when the full rescattering contribution is included, the $pp\gamma$ cross section will show an ω dependence similar to the $pn\gamma$ process over all of the photon energy region [compare Figs. 3 and 12(a)]. Moreover, the photon cross section here exhibits a much stronger incident energy dependence than in the $pn\gamma$ process and it is not restricted to the low photon energy region. This different behavior of the $pp\gamma$ cross section compared to that of pn bremsstrahlung is caused, in part, by the different incident energy dependence of pp and np T matrices. Recall that the pp total cross section has a much weaker energy dependence than the np cross section. Another reason for the different incident energy dependence between pp and pn bremsstrahlung is the absence of the two-body current contribution in the $pp\gamma$ process. A comparison of Figs. 5 and 13 also shows that convection current contribution is strongly suppressed in going from the $pn\gamma$ to the $pp\gamma$ process. This is easy to understand because, in the latter process, the convection currents associated with the two interacting protons cancel to a large extent, while in the former process it does not. The magnetization current contribution for $pp\gamma$ is comparable to $pn\gamma$ bremsstrahlung. The pp cross section is smaller than the np total cross section, but this is compensated by both a larger magnetic moment of the proton and by the spin matrix elements of $\sigma\cdot(\hat{\mathbf{k}}\wedge\boldsymbol{\epsilon})$. The latter weights each two-body partial-wave state differently. As a result, the relative importance of the individual current contribution is different for pp and pn bremsstrahlung. In the $pp\gamma$ case the magnetic contribution largely dominates the convection contribution at much lower photon energies than in the $pn\gamma$ process. Moreover, the one-body current contribution to the $pp\gamma$ cross section becomes comparable to that of $pn\gamma$ for sufficiently high incident energies. However, the total contribution is much smaller in pp bremsstrahlung than in pn bremsstrahlung. At $T_{\rm lab}=150$ MeV, the $pp\gamma$ cross section is more than an order of magnitude smaller than the corresponding $pn\gamma$ cross section; at $T_{\rm lab}=600$ MeV it is still a factor of ~ 4 smaller. This is due to the large two-body current contribution, which is mostly absent in the $pp\gamma$ case.

In Fig. 14 the angular distributions at $T_{\rm lab}=600$ MeV and for various photon energies are shown. They are symmetric with respect to $\theta=90°$ because of the identity of the protons. We see the remarkable change in the angular distribution as the photon energy increases. For low ω the angular distribution exhibits a pronounced quadrupole shape; it is entirely dominated by the convection contribution. As ω increases, the angular distribution changes to a $\cos^2\theta$ dependence because of the increasing contribution of the magnetic current.

As in the previous subsection, these features can be understood by examining the external current contribution. Analogous to what we have obtained for the $pn\gamma$ cross sections [Eqs. (3.1) and (3.2)], where we obtain, to leading order,

$$\frac{d^2\sigma_{\rm conv}}{d\omega\, d\Omega}=\frac{\alpha}{(2\pi)^2}\frac{1}{\omega}\left[\frac{p'}{p}\right]\left[\frac{\varepsilon(p')\varepsilon(p)T_{pp}^2}{8\pi}\right]\times\left(\tfrac{8}{15}v'^4+v^4\sin^2 2\theta\right) \tag{3.4}$$

for the convection current contribution and

$$\frac{d^2\sigma_{\rm magn}}{d\omega\, d\Omega}=\frac{\alpha}{(2\pi)^2}\frac{\omega}{m^2}\left[\frac{p'}{p}\right]\left[\frac{\varepsilon(p')\varepsilon(p)T_{pp}^2}{8\pi}\right]\mu_p^2\times\left[[(g-d)^2+\tfrac{1}{3}g^2v'^2]+d^2v^2\cos^2\theta\right] \tag{3.5}$$

for the magnetic contribution. In the above equations,

the quantity in the large parentheses becomes the pp total cross section (σ_{pp}) in the SPA limit.

The convection current contribution now has a quadrupole shape. It also shows a v^4 dependence, which is a different incident energy dependence than for the corresponding $pn\gamma$ cross section [Eq. (3.1)], as we have observed before. The magnetic contribution gives a $\cos^2\theta$ dependence. Unlike the $pn\gamma$ case [Eq. (3.2)], the linear term in $\cos\theta$ is absent here because of the identity of the two interacting particles. Equations (3.4) and (3.5) explain the qualitative feature of the angular distribution in Fig. 14. The deviations observed there from Eqs. (3.4) and (3.5) are due to the higher-order corrections which were neglected in Eqs. (3.4) and (3.5). For lower incident energies, the angular distribution will become less pronounced as can be seen from Eqs. (3.4) and (3.5).

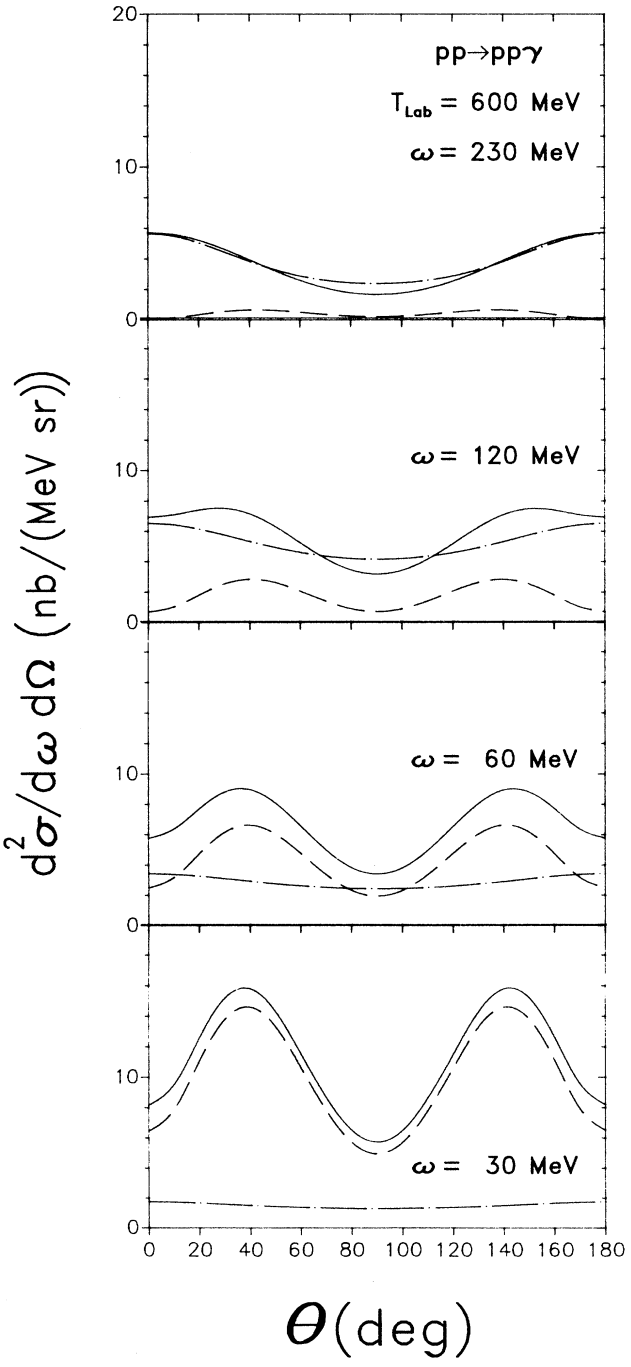

FIG. 14. $pp\gamma$ angular distribution in the initial proton-proton center-of-mass frame at $T_{\rm lab}=600$ MeV. The photon energies are, from bottom to top, $\omega=30$, 60, 120, and 230 MeV. For further details, see the caption of Fig. 12(a).

A rough estimate of the ratio between the $pp\gamma$ and $pn\gamma$ cross sections can be obtained from Eqs. (3.1) and (3.2) and Eqs. (3.4) and (3.5). For the convection contribution in the SPA and at $\theta=0°$, it yields

$$R_c=\frac{4}{5}\left[\frac{\sigma_{pp}}{\sigma_{np}}\right]v^2 . \tag{3.6}$$

This shows that, for the convection contribution, the $pp\gamma$ cross section is much smaller than the $pn\gamma$ cross section for low incident energies. In addition to the factor v^2, the np total cross section (σ_{np}) is much larger than the pp cross section σ_{pp}. As the incident energy increases, the ratio R_c increases, not only due to the factor v^2 but also due to the fact that σ_{np} decreases much more rapidly than σ_{pp} with incident energy, as has already been discussed. Assuming that the ratio between the pp and np total cross sections becomes unity for very high incident energies, we see that the ratio R_c tends to the limit $\frac{4}{5}$ at $\theta=0°$. Similarly, for the magnetic contribution, we obtain the ratio

$$R_m\sim\frac{2\mu_p^2}{\mu_p^2+\mu_n^2}\left[\frac{\sigma_{pp}}{\sigma_{np}}\right]\sim\sqrt{2}\left[\frac{\sigma_{pp}}{\sigma_{np}}\right], \tag{3.7}$$

at $\theta=90°$, assuming the parameters d and g to be the same for $pp\gamma$ and $pn\gamma$. In that case, the $pp\gamma$ cross section may become larger than the corresponding $pn\gamma$ cross section for sufficiently high incident energies where σ_{pp} becomes comparable to σ_{np}. However, in the region of incident energy where the present potential model is applicable ($T_{\rm lab}<300$ MeV), the pp bremsstrahlung is smaller than the pn bremsstrahlung by a factor of ~ 5 or more. The nn bremsstrahlung contribution can be obtained from the magnetization current contribution from pp bremsstrahlung by multiplying that result by $(\mu_n/\mu_p)^2$.

C. Parametrization of the $pn\gamma$ amplitude

In this subsection we give a simple parametrization of the $pn\gamma$ amplitude which may be useful in the application of the present formalism to more complicated processes such as nucleon-nucleus and/or heavy-ion scattering.

Following Ref. 12, we write the $pn\gamma$ transition amplitude for the convection current contribution as

$$\langle \epsilon,\mathbf{k};\mathbf{p}'S'M_{S'}|V_{\rm conv}|0;\mathbf{p}SM_S\rangle \simeq \sqrt{(2\pi)/k}\,\frac{1}{\omega}T(E_{\rm c.m.},\omega)\delta_{SS'}\delta_{M_SM_{S'}} \times\left[-e_1\left[\frac{\epsilon\cdot\mathbf{v}'}{1-\hat{\mathbf{k}}\cdot\mathbf{v}'}-\frac{\epsilon\cdot\mathbf{v}}{1-\hat{\mathbf{k}}\cdot\mathbf{v}}\right]+e_2\left[\frac{\epsilon\cdot\mathbf{v}'}{1+\hat{\mathbf{k}}\cdot\mathbf{v}'}-\frac{\epsilon\cdot\mathbf{v}}{1+\hat{\mathbf{k}}\cdot\mathbf{v}}\right]\right], \tag{3.8}$$

and for the magnetization current contribution as

$$\langle \epsilon,\mathbf{k};\mathbf{p}'S'M_{S'}|V_{\rm magn}|0;\mathbf{p}SM_S\rangle \simeq i\sqrt{(2\pi)/k}\left[\frac{e}{2m}\right]T(E_{\rm c.m.},\omega) \times\left[\mu_1\left[\frac{g(E_{\rm c.m.})}{1-\hat{\mathbf{k}}\cdot\mathbf{v}'}-\frac{d(E_{\rm c.m.})}{1-\hat{\mathbf{k}}\cdot\mathbf{v}}\right]+\mu_2(-)^{S'-S}\left[\frac{g(E_{\rm c.m.})}{1+\hat{\mathbf{k}}\cdot\mathbf{v}'}-\frac{d(E_{\rm c.m.})}{1+\hat{\mathbf{k}}\cdot\mathbf{v}}\right]\right] \times\langle S'M_{S'}|\sigma_1\cdot(\hat{\mathbf{k}}\wedge\epsilon)|SM_S\rangle\ . \tag{3.9}$$

In the above equations $\mathbf{v}'(\mathbf{v})$ is the velocity of the nucleon associated with $\mathbf{p}'(\mathbf{p})$ in units of c. $T(E_{\rm c.m.},\omega)$ denotes the angle- and spin-averaged T-matrix element; it depends on two variables which can be taken as the initial NN c.m. energy $E_{\rm c.m.}$ and the photon energy ω. In Eq. (3.9), $d(E_{\rm c.m.})$ and $g(E_{\rm c.m.})$ are parameters introduced because we assumed the T matrix to be diagonal in spin-projection quantum numbers. Here the magnetic contribution differs from that of Ref. 12 because it contains an extra parameter $g(E_{\rm c.m.})$ which improves the description of the angular distribution where the magnetization current dominates over the other currents. In the limit of $g=d$, Eq. (3.9) reduces to that of Ref. 12.

The two-body current amplitude is parametrized as in Ref. 12:

$$\langle \epsilon,\mathbf{k};\mathbf{p}'S'M_{S'}|V_{\rm exch}|0;\mathbf{p}SM_S\rangle \simeq -2e\sqrt{(2\pi)/k}\left[\frac{f}{\mu}\right]^2\frac{\langle T'0|i/2(\tau_1\wedge\tau_2)_z|T0\rangle}{q^2+\mu^2} \times\langle S'M_{S'}|\left[2\epsilon\cdot\mathbf{q}\frac{\sigma_1\cdot\mathbf{q}\sigma_2\cdot\mathbf{q}}{q^2+\mu^2}-(\sigma_1\cdot\epsilon\sigma_2\cdot\mathbf{q}+\sigma_1\cdot\mathbf{q}\sigma_2\cdot\epsilon)\right]|SM_S\rangle\ , \tag{3.10}$$

where $\mathbf{q}=\mathbf{p}'-\mathbf{p}$ denotes the momentum transfer. The mass of the effective meson exchanged (μ) and the coupling strength (f) are parameters in the above equation. The isospin matrix element, which takes the value $+1$ or -1 according to $T=0$, $T'=1$ or $T=1$, $T'=0$, we assume to be $+1$.

We fit Eqs. (3.8)–(3.10) to the pn bremsstrahlung cross sections as calculated in Sec. III A. For a given initial energy of the nucleon in the NN c.m. system, the quantities T in Eqs. (3.8) and (3.9) and f^2 in Eq. (3.10) have been parametrized as linear functions of the photon energy ω:

$$T(E_{\rm c.m.},\omega)=a(E_{\rm c.m.})[1+b(E_{\rm c.m.})\omega]\ , \qquad \left[\frac{f(E_{\rm c.m.},\omega)}{\mu}\right]^2=a'(E_{\rm c.m.})[1+b'(E_{\rm c.m.})\omega]\ . \tag{3.11}$$

The mass of the effective meson exchanged has been fixed to be the pion mass, i.e., $\mu=0.7\ {\rm fm}^{-1}$.

In Table III the results are given for incident energies up to $T_{\rm lab}=800$ MeV. As mentioned at the beginning of this section, since the bare NN potential used does not include inelasticity, one has a limitation on the maximum incident energy for which the present model is strictly applicable ($T_{\rm lab}<300$ MeV). Therefore, we must keep this fact in mind when applying the present results to higher energies. The quality of the present fit to the exact calculation is essentially the same as that of Ref. 12, except for the magnetization contribution, whose angular distribution is now much better described. This is reflected in the values of d and g which take different values from each other.

IV. CONCLUSION

The present calculation yields both pp and np bremsstrahlung exclusive cross sections which are in excellent agreement with some of the earlier calculations, provided the NN transition amplitudes of Refs. 10 and 24 are multiplied by the factor $\sqrt{m/\varepsilon_{p'}}\sqrt{m/\varepsilon_p}$ which is required for constructing Lorentz scalar amplitudes.

In the present work we have extended the investigation of NN bremsstrahlung for producing energetic photons in an effort to provide a more reliable basis for photoproduction calculations in heavy-ion collisions, paying special attention to the rescattering contribution from the one-body current, whose exact evaluation requires a considerable numerical effort. The SPA [Eq. (2.8)] and MSPA [Eq. (2.12)] are in excellent agreement with exact calculations, thus simplifying the evaluation of this contribution. It has also been shown that the one-body rescattering contribution for inclusive cross sections is relevant only in the region of photon energy near its end point. Moreover, we found that the dominant contribution arises from the magnetic current.

The $pn\gamma$ double-differential cross section is found to be rather insensitive to the incident energy, except in the low photon energy region, where it is entirely dominated by the convection current contribution. This insensitivity

is due to the fact that the two-body current contribution decreases as the incident energy increases while the convection contribution increases. The convection current contribution gives rise to a very pronounced angular dependence, which is not the case for the magnetization and two-body current contributions. As a result, for incident energies up to $T_{\rm lab} \sim 300$ MeV, the angular distribution is determined by the convection current which gives essentially the well-known dipole shape. For a fixed incident energy, the angular dependence becomes less pronounced as the photon energy increases because of the suppression of the convection contribution. At higher incident energies (where very high-energy photons can be created) the angular distribution changes from a $\sin^2\theta$ to a $\cos^2\theta$ shape as the photon energy increases due to the magnetization current contribution. The internal current (one-body rescattering plus two-body current) contribution has a nearly isotropic angular distribution. The present calculation yields $np\gamma$ cross sections which still tend to underpredict the data, in spite of large uncertainties in the experimental data. For the $np\gamma$ total cross section there is a clear incompatibility with the data of Ref. 20 at $T_{\rm lab}=140$ MeV.

The pp bremsstrahlung inclusive cross section for a fixed photon emission angle is found to have similar features to those of the $pn\gamma$ process as a function of photon energy. However, in contrast to the pn bremsstrahlung, the $pp\gamma$ cross section increases as a function of incident energy due to the absence of the two-body current contribution. Also, the magnetic current contribution is relatively much more important than the convection term compared with the $pn\gamma$ case; the convection contribution is largely suppressed while the magnetic contribution remains comparable to that in the pn bremsstrahlung. For a given incident energy the angular distribution has a quadrupole shape for low photon energies, where it is dominated by the convection term. As the photon energy increases, the cross section becomes dominated by the magnetic contribution, and the shape of the angular distribution changes to a $\cos^2\theta$ form. The $pp\gamma$ cross section is small compared with that from the $pn\gamma$ process, even for photon energies as high as $\omega=200$ MeV, where it is still a factor of ~ 5 smaller than the $pn\gamma$ cross section. This relatively small $pp\gamma$ cross section is due to the near absence of a two-body current in this case. Therefore, in calculations where no interference occurs between the $pp\gamma$ and $pn\gamma$ processes (such as in existing heavy-ion data), we may consider only the latter process. As in pn bremsstrahlung there is, to our knowledge, only one set of pp bremsstrahlung inclusive cross-section data (Rothe *et al.*[29]). Our calculation reproduces the slope of the spectrum[29] but yields a cross section which is too large by a factor of ~ 2. Similar results have also been obtained in earlier calculations.[30,31]

It is clear that more data are required for both pp and np bremsstrahlung in order to test existing potential model calculations, especially in geometries where photon energies near the maximum value allowed kinematically can be reached. Such an experiment has been recently proposed by the Jülich group at COSY.[32]

We should mention that the present calculation preserves the gauge invariance only in the SPA, for it includes the two-body current contribution only in that limit (we have seen that the one-body rescattering contribution is considerable only beyond the SPA). However, as mentioned before, this may not be critical for calculating inclusive cross sections. It is certainly very important to learn about the role of the two-body contribution, beyond the SPA, in producing energetic photons. Theoretically, this is one of the present limitations in using the np bremsstrahlung as a tool for investigating, for example, the off-energy-shell effects of the NN interaction.

Finally, we remember that in the present calculation no inelasticities have been included. Therefore, the results we have presented for incident energies beyond the pion threshold should be interpreted with caution. The present calculation also uses the nonrelativistic electromagnetic current operator; for high incident ($T_{\rm lab} \geq 200$ MeV) and photon energies, relativistic spin corrections may become considerable.[15,16]

ACKNOWLEDGMENTS

We are indebted to Virginia Brown for many discussions and also for helping check the numerical results. We thank Hugo Arellano for providing us with a computer code for calculating the T-matrix elements based on the Hamada-Johnston potential which allowed us to make a close comparison with earlier calculations. We also thank W. G. Love and J. Durso for a careful reading of the manuscript. One of us (V.H.) acknowledges partial support received from the Department of Physics and Astronomy during his stay at the University of Georgia. This work was supported in part by North Atlantic Treaty Organization (NATO) Grant RG85/0093. We also appreciate a grant for computing time provided by the University Computing and Networking Services of the University of Georgia.

APPENDIX A

As far as the momentum integration is concerned, Eq. (2.3) as well as Eq. (2.9) is of the form

$$R = \int d^3p'' \frac{F(\mathbf{p}'')}{D_{\pm} E(p'',p)} , \tag{A1}$$

where $D_{\pm}$ and $E(p'',p)$ are defined in Eq. (2.5).

We perform the above integral first integrating over the magnitude of $\mathbf{p}''$ ("radial" integral) and then integrate over the solid angle, i.e.,

$$R = \int d\Omega'' \int_0^{\infty} dp'' p''^2 \frac{F(\mathbf{p}'')}{D_{\pm} E(p'',p)} . \tag{A2}$$

For a given solid angle Ω'', the "radial" integral has two simple poles: one at $E(p'',p)=0$ and another at $D_{\pm}=0$. Therefore, we split the integral in two pieces, each containing only one pole (this is always possible since they are simple poles) and write it as

$$X(\hat{\mathbf{p}}'')\equiv\int_0^\infty dp''p''^2\frac{F(p'')}{D_\pm E(p'',p)}$$
$$=\int_0^a dp''p''^2\frac{F(p'')}{D_\pm E(p'',p)}$$
$$+\int_a^\infty dp''p''^2\frac{F(p'')}{D_\pm E(p'',p)}\ , \tag{A3}$$

where a is chosen such that the first integral contains a pole from $D_\pm$ and the second one a pole from $E(p'',p)$. In the above equation we have omitted explicit reference to the angular part of $\mathbf{p}''$.

The second integral in Eq. (A3) can be evaluated most easily if we write the relevant energy denominator as

$$\frac{1}{E(p'',p)}=\frac{1}{2}\left[\frac{\varepsilon(p'')+\varepsilon(p)}{p^2-p''^2+i\eta}\right]\ . \tag{A4}$$

Inserting this into the second integral, we obtain

$$X_2(\hat{\mathbf{p}}'')\equiv\int_a^\infty dp''p''^2\frac{F(p'')}{D_\pm E(p'',p)}$$
$$=\int_a^\infty dp''\frac{A(p'')}{p^2-p''^2+i\eta}$$
$$=\int_a^\infty dp''\frac{A(p'')-A(p)}{p^2-p''^2}$$
$$+\frac{A(p)}{2p}\ln\left|\frac{p-a}{p+a}\right|-i\pi\frac{A(p)}{2p}\ , \tag{A5a}$$

where, in the last step, we have subtracted and added a term in order to smooth the integrand for numerical purposes. We have also introduced the notation

$$A(p'')=p''^2\frac{[\varepsilon(p'')+\varepsilon(p)]F(p'')}{2D_\pm}\ . \tag{A5b}$$

In order to perform the first integral in Eq. (A3), we define the quantity $p'_\pm$ through the relation

$$\varepsilon(p'_\pm)+\varepsilon(|\mathbf{p}'_\pm\pm\mathbf{k}|)=\varepsilon(|\mathbf{p}'-\mathbf{k}/2|)+\varepsilon(|\mathbf{p}'+\mathbf{k}/2|)\ , \tag{A6a}$$

with the condition

$$\hat{\mathbf{p}}'_\pm=\hat{\mathbf{p}}'' \tag{A6b}$$

so that the energy denominator $D_\pm$ can be written in the more symmetric form

$$D_\pm=\varepsilon(p'_\pm)+\varepsilon(|\mathbf{p}'_\pm\pm\mathbf{k}|)-\varepsilon(p'')-\varepsilon(|\mathbf{p}''\pm\mathbf{k}|)+i\eta\ . \tag{A7}$$

We then proceed similarly to the previous case to write

$$X_1(\hat{\mathbf{p}}'')\equiv\int_0^a dp''p''^2\frac{F(p'')}{D_\pm E(p'',p)}$$
$$=\int_0^a dp''\left[\frac{B(p'')}{D_\pm}-\frac{B(p'_\pm)}{2(p'^2_\pm-p''^2)}\right]$$
$$+\frac{B(p'_\pm)}{4p'_\pm}\ln\left|\frac{p'_\pm+a}{p'_\pm-a}\right|-i\pi\frac{B(p'_\pm)}{4p'_\pm}\ . \tag{A8a}$$

Here

$$B(p'')=p''^2\frac{F(p'')}{E(p'',p)}\ . \tag{A8b}$$

It may happen that Eq. (A6a) cannot be satisfied for some direction $\hat{\mathbf{p}}'_\pm$ given by Eq. (A6b). In this case the integrand in $X_1(\hat{\mathbf{p}}'')$ contains no pole and, consequently, there is no problem with the numerical integration.

APPENDIX B

In this appendix we construct the Lorentz-invariant transition amplitude from the nonrelativistic NN T matrix. The nonrelativistic T matrix ($T_{\rm nr}$) obeying the Schrödinger equation (or the Lippmann-Schwinger equation) is related to the cross section in the NN c.m. system by

$$\frac{d\sigma}{d\Omega}=\left[\frac{m}{4\pi}\right]^2|T_{\rm nr}(\mathbf{p}',\mathbf{p})|^2\ , \tag{B1}$$

with the final and initial relative momenta, $\mathbf{p}'$ and $\mathbf{p}$, obeying $|\mathbf{p}'|=|\mathbf{p}|$. This is the case, for example, of the T matrices based on the Paris and Hamada-Johnston potentials. Now we want to construct the Lorentz-invariant transition amplitude from $T_{\rm nr}(\mathbf{p}',\mathbf{p})$. The total NN cross section in terms of invariant quantities can be written as

$$\sigma=\left[\frac{1}{\varepsilon_1\varepsilon_2[(\boldsymbol{\beta}_1-\boldsymbol{\beta}_2)^2-(\boldsymbol{\beta}_1\times\boldsymbol{\beta}_2)^2]^{1/2}}\right]$$
$$\times\int\frac{d^3p'_1}{\varepsilon'_1(2\pi)^3}\int\frac{d^3p'_2}{\varepsilon'_2(2\pi)^3}|\sqrt{\varepsilon'_1\varepsilon'_2}T(\mathbf{p}_{1'},\mathbf{p}_{2'};\mathbf{p}_1,\mathbf{p}_2)\sqrt{\varepsilon_1\varepsilon_2}|^2(2\pi)^4\delta(\mathbf{p}_1+\mathbf{p}_2-\mathbf{p}'_1-\mathbf{p}'_2)\delta(\varepsilon_1+\varepsilon_2-\varepsilon'_1-\varepsilon'_2)\ . \tag{B2}$$

In the above equation, $\mathbf{p}_i$ and $\varepsilon_i=(\mathbf{p}_i^2+m^2)^{1/2}$ denote the momentum and energy of the nucleon i in the initial state, respectively; $\boldsymbol{\beta}_i=\mathbf{p}_i/\varepsilon_i$. The primed quantities refer to the final state.

The quantity

$$\tilde{T}(\mathbf{p}_{1'},\mathbf{p}_{2'};\mathbf{p}_1,\mathbf{p}_2)=(\varepsilon'_1\varepsilon'_2)^{1/2}T(\mathbf{p}_{1'},\mathbf{p}_{2'};\mathbf{p}_1,\mathbf{p}_2)(\varepsilon_1\varepsilon_2)^{1/2} \tag{B3}$$

is the Lorentz-invariant NN transition amplitude and we now look for a relationship between T in the above equa-

tion and $T_{\rm nr}$ in Eq. (B1).

In the NN c.m. frame, Eq. (B2) reduces to

$$\sigma=\frac{1}{4\varepsilon_p^2}\frac{1}{(2\pi)^2}\int d\Omega|\sqrt{\varepsilon_{p'}\varepsilon_{p'}}T(\mathbf{p}',\mathbf{p})\sqrt{\varepsilon_p\varepsilon_p}|^2 \quad \text{(B4)}$$

with $\varepsilon_{p'}=\varepsilon_p=(\mathbf{p}^2+m^2)^{1/2}$. Therefore, we have

$$\frac{d\sigma}{d\Omega}=\left[\frac{m}{4\pi}\right]^2|\sqrt{\varepsilon_p/m}\,T(\mathbf{p}',\mathbf{p})\sqrt{\varepsilon_p/m}\,|^2 . \quad \text{(B5)}$$

Comparing Eqs. (B1) and (B5) yields

$$T(\mathbf{p}',\mathbf{p})=\sqrt{m/\varepsilon_p}\,T_{\rm nr}(\mathbf{p}',\mathbf{p})\sqrt{m/\varepsilon_p} . \quad \text{(B6)}$$

Of course, Eq. (B6) is valid only on-the-energy-shell, i.e., $|\mathbf{p}'|=|\mathbf{p}|$. Off-the-energy-shell ($|\mathbf{p}'|\neq|\mathbf{p}|$) the extension of Eq. (B6) is

$$T(\mathbf{p}',\mathbf{p})=\sqrt{m/\varepsilon_{p'}}\,T_{\rm nr}(\mathbf{p}',\mathbf{p})\sqrt{m/\varepsilon_p} , \quad \text{(B7)}$$

which is the desired result. We note that, in the case of the OBEPQ version of the Bonn potential, where the Lorentz structure of the interaction is known (this potential is based on the relativistic meson-exchange theory) and that the resulting Blankenbecler-Sugar equation (which is obtained from a three-dimensional reduction of the Bethe-Salpeter equation) can be cast into a Lippmann-Schwinger equation by a proper redefinition of the NN interaction,[17] the Lorentz scalar nature of $\tilde{T}$ in Eq. (B3) with T given by Eq. (B7) can be explicitly verified. We also observe that Eq. (B1) is obtained by imposing the unitarity of the S matrix associated with $T_{\rm nr}$; therefore, if we use $T_{\rm nr}$ instead of T given by Eq. (B6) in Eq. (B2), we violate the unitarity of the S matrix.

Since we also express the bremsstrahlung transition amplitude in terms of Lorentz-invariant amplitude,[10,11,24] the T matrix required in such calculations is that given by Eq. (B7) and not $T_{\rm nr}$. In order to see this explicitly, we consider, for simplicity, the bremsstrahlung transition amplitude from the convection current as given in Ref. 11. Moreover, we restrict to the term in which the photon is emitted by one of the interacting nucleons, say, nucleon 1, before the strong interaction takes place. This corresponds to the first term in Eq. (2.7a) of Ref. 11 and we will denote this amplitude by

$$\langle\boldsymbol{\epsilon},\mathbf{k};\mathbf{p}_{1'}\mathbf{p}_{2'}S'M_{S'}|V_{\rm conv}|0;\mathbf{p}_{1''}\mathbf{p}_{2''}SM_S\rangle .$$

Then, according to Ref. 11, the invariant amplitude is given by

$$\tilde{V}_{\rm conv}=\sqrt{\varepsilon_{1'}\varepsilon_{2'}\omega}\langle\boldsymbol{\epsilon},\mathbf{k};\mathbf{p}_{1'}\mathbf{p}_{2'}S'M_{S'}|V_{\rm conv}|0;\mathbf{p}_{1''}\mathbf{p}_{2''}SM_S\rangle\sqrt{\varepsilon_{1''}\varepsilon_{2''}} . \quad \text{(B8)}$$

We want to verify explicitly that the above amplitude is, in fact, a Lorentz invariant. In the final NN c.m. frame, following Ref. 11, we have

$$\tilde{V}_{\rm conv}=\sqrt{\varepsilon_{1'}\varepsilon_{2'}\omega}\left[-e_1\sqrt{(2\pi)/k}\,\delta_{SS'}\frac{\boldsymbol{\epsilon}\cdot\mathbf{p}}{m}\frac{\langle\mathbf{p}',S'M_{S'}|(T^-)^\dagger|\mathbf{p}-\mathbf{k}/2,SM_S\rangle}{E(|\mathbf{p}-\mathbf{k}/2|,\mathbf{p})}\right]\sqrt{\varepsilon_{1''}\varepsilon_{2''}} , \quad \text{(B9)}$$

where $E(|\mathbf{p}-\mathbf{k}/2|,p')$ is defined by Eq. (2.5c); $\varepsilon_{1'}=\varepsilon_{2'}=\varepsilon_{p'}$ and $\varepsilon_{1''}=\varepsilon_{2''}=\varepsilon_{|\mathbf{p}-\mathbf{k}/2|}$.

Using Eq. (B3), the above expression can be rewritten as

$$\tilde{V}_{\rm conv}=-e_1\sqrt{2\pi}\delta_{SS'}\frac{\boldsymbol{\epsilon}\cdot\mathbf{p}}{m}\frac{\langle S'M_{S'}|(\tilde{T}^-)^\dagger(\mathbf{p}',\mathbf{p}-\mathbf{k}/2)|SM_S\rangle}{E(|\mathbf{p}-\mathbf{k}/2|,p')} . \quad \text{(B10)}$$

The quantity $\boldsymbol{\epsilon}\cdot\mathbf{p}$ in the above equation can be rewritten as

$$\boldsymbol{\epsilon}\cdot\mathbf{p}=\boldsymbol{\epsilon}\cdot\mathbf{p}-\epsilon^0p_0=-\epsilon^\mu p_\mu , \quad \text{(B11)}$$

since we work in a gauge where $\epsilon^0=0$. ϵ^μ and p_μ are four vectors. Also, it is easy to see that the energy denominator can be reexpressed as

$$\begin{aligned}E(|\mathbf{p}-\mathbf{k}/2|,p')&=2[\varepsilon(p')-\varepsilon(|\mathbf{p}-\mathbf{k}/2|)]\\&=\{[2\varepsilon(p')]^2-\mathbf{P}'^2\}^{1/2}-\{[2\varepsilon(|\mathbf{p}-\mathbf{k}/2|)]^2-\mathbf{P}'^2\}^{1/2}\\&=[(\varepsilon_{1'}+\varepsilon_{2'})^2-\mathbf{P}'^2]^{1/2}-[(\varepsilon_{1''}+\varepsilon_{2''})^2-\mathbf{P}'^2]^{1/2} , \quad \text{(B12)}\end{aligned}$$

where

$$\mathbf{P}'=\mathbf{p}_{1'}+\mathbf{p}_{2'}=\mathbf{p}_{1''}+\mathbf{p}_{2''}=0 \quad \text{(B13)}$$

is the final NN c.m. momentum. The quantities

$$\begin{aligned}s'&\equiv(\varepsilon_{1'}+\varepsilon_{2'})^2-\mathbf{P}'^2=(p_{1'}+p_{2'})^\mu(p_{1'}+p_{2'})_\mu ,\\ s''&\equiv(\varepsilon_{1''}+\varepsilon_{2''})^2-\mathbf{P}'^2=(p_{1''}+p_{2''})^\mu(p_{1''}+p_{2''})_\mu ,\end{aligned} \quad \text{(B14)}$$

in Eq. (B12) are Lorentz scalars.

Using Eqs. (B11)–(B14) in Eq. (B10), we obtain

$$\tilde{V}_{\rm conv}=e_1\sqrt{2\pi}\delta_{SS'}\frac{\epsilon^\mu p_\mu}{m}\frac{\langle S'M_{S'}|(\tilde{T}^-)^\dagger|SM_S\rangle}{(s')^{1/2}-(s'')^{1/2}} , \quad \text{(B15)}$$

which is, manifestly, Lorentz invariant provided $\tilde{T}$, T, and $T_{\rm nr}$ are related via Eqs. (B3) and (B7). In other words, $\tilde{V}_{\rm conv}$ will be Lorentz invariant if the NN transition amplitude $\tilde{T}$ is a Lorentz invariant. The same conclusion follows for other terms in the bremsstrahlung amplitude.

[1]E. Grosse, P. Grimm, H. Heckwolf, W. F. J. Mueller, H. Noll, A. Oskarsson, H. Stelzer, and W. Roesch, Europhys. Lett. **2**, 9 (1986).
[2]J. Stevenson *et al.*, Phys. Rev. Lett. **57**, 555 (1986).
[3]N. Alamanos, P. Braun-Munzinger, R. H. Freifelder, P. Paul, J. Stachel, T. C. Awes, R. L. Fergusson, F. E. Obenshain, F. Plasil, and G. R. Young, Phys. Lett. B **173**, 392 (1986).
[4]K. Kwato Njock, M. Maurel, E. Monnand, H. Nifenecker, J. A. Pinston, F. Schussler, and D. Barneoud, Phys. Lett. B **175**, 125 (1986).
[5]T. S. Biro, K. Niita, A. A. DePaoli, W. Bauer, W. Cassing, and U. Mosel, Nucl. Phys. **A475**, 579 (1987).
[6]B. A. Remington, M. Blann, and G. F. Bertsch, Phys. Rev. C **35**, 1720 (1987).
[7]C. M. Ko and J. Aichelin, Phys. Rev. C **35**, 1976 (1987).
[8]R. Heuer, B. Müller, H. Stoecker, and W. Greiner, Z. Phys. A **330**, 315 (1988).
[9]L. S. Celenza *et al.*, Phys. Lett. **41B**, 283 (1972).
[10]V. R. Brown and J. Franklin, Phys. Rev. C **8**, 1706 (1973).
[11]K. Nakayama, Phys. Rev. C **39**, 1475 (1989).
[12]K. Nakayama and G. F. Bertsch, Phys. Rev. C **40**, 685 (1989).
[13]M. K. Liou and M. I. Sobel, Phys. Rev. C **4**, 1507 (1971).
[14]R. A. Brandenburg, G. S. Chulik, R. Machleidt, A. Pickelsimer, and R. M. Thaler, Phys. Rev. C **37**, 1245 (1988).
[15]R. L. Workman and H. W. Fearing, Phys. Rev. C **34**, 780 (1986).
[16]H. W. Fearing, Nucl. Phys. **A463**, 95c (1987).
[17]K. Nakayama and W. G. Love, Phys. Rev. C **38**, 51 (1988).
[18]F. P. Brady and J. C. Young, Phys. Rev. C **2**, 1579 (1970); **7**, 1707 (1973).
[19]P. F. M. Koehler, K. W. Rothe, and E. H. Thorndike, Phys. Rev. Lett. **18**, 933 (1967).
[20]J. Edgington and B. Rose, Nucl. Phys. **89**, 523 (1966).
[21]H. Nifenecker, M. Kwato Njock, and J. A. Pinston, Nucl. Phys. **A495**, 3c (1989).
[22]K. Nakayama and G. F. Bertsch, Phys. Rev. C **40**, 2520 (1989).
[23]B. A. Remington, M. Blann, and G. F. Bertsch, Phys. Rev. Lett. **57**, 2909 (1986); Phys. Rev. C **35**, 1720 (1987).
[24]V. R. Brown, Phys. Rev. **177**, 1498 (1969).
[25]D. Drechsel and L. C. Maximon, Ann. Phys. (N.Y.) **49**, 403 (1968).
[26]B. Gottschalk, W. J. Schlaer, and K. H. Wang, Nucl. Phys. **A94**, 491 (1967).
[27]C. A. Smith, J. V. Jovanovich, and L. G. Greeniaus, Phys. Rev. C **22**, 2287 (1980).
[28]H. W. Fearing, Phys. Rev. C **22**, 1388 (1980).
[29]K. W. Rothe, P. F. M. Koehler, and E. H. Thorndike, Phys. Rev. **157**, 1247 (1966).
[30]E. M. Nyman, Phys. Rev. **170**, 1628 (1968).
[31]Y. Ueda, Phys. Rev. **145**, 1214 (1966).
[32]E. Kuhlmann and H. P. Morsh (unpublished).